



UKAEA-CCFE-PR(25)354

Lynton Appel

Analytic model for the propagation of a collisionless Neutral beam

Enquiries about copyright and reproduction should in the first instance be addressed to the UKAEA Publications Officer, Culham Science Centre, Building K1/0/83 Abingdon, Oxfordshire, OX14 3DB, UK. The United Kingdom Atomic Energy Authority is the copyright holder.
The contents of this document and all other UKAEA Preprints, Reports and Conference Papers are available to view online free at scientific-publications.ukaea.uk/

Analytic model for the propagation of a collisionless Neutral beam

Lynton Appel







Analytic model for the propagation of a collisionless neutral beam

UKAEA (United Kingdom Atomic Energy Authority), Culham Campus, Abingdon, Oxfordshire, OX14 3DB

Lynton Appel

Abstract

This paper introduces an analytical model for the propagation of collisionless neutral particles in neutral beam injection (NBI) systems. The model incorporates a novel approach using composite Gaussian basis functions to represent non-Gaussian source distributions and extends to two-dimensional source configurations under orthogonal separability assumptions. The method efficiently computes particle velocity and spatial distributions along beam trajectories, accounting for truncation effects due to transmission losses. The model has been implemented as a computational module in the Minerva framework and interfaced with the ITER Integrated Modelling & Analysis Suite (IMAS).

A case study of the MAST Upgrade NBI system demonstrates the model's ability to predict particle distributions from the source grid to the plasma cavity while accommodating detailed baffle geometries and calculating transmission factors. Comparisons reveal that reduced Gaussian basis representations can achieve an order-of-magnitude reduction in computational time with negligible impact on accuracy. The proposed model provides a fast and rigorous alternative to Monte Carlo simulations, enabling enhanced diagnostic modelling and efficient integration with Bayesian inference frameworks.

Keywords: neutral beam, NBI, probability, distribution, magnetic confinement fusion, Bayesian,

1. Introduction

High-energy neutral beam systems play a vital role in the current generation of tokamak and stellarator magnetic confinement devices, serving both as a key mechanism for plasma heating and current drive [1] and as a valuable diagnostic tool for plasma quantities [2, 3]. In this paper we consider the propagation of a collisionless particle beam distribution as a precursor to its modification by collisions with populations of neutrals and ions. Here the challenge lies in achieving a fast and accurate analysis involving integrals over 6-dimensional phase space (i.e. three spatial and three in velocity) whilst simultaneously including details of a realistic geometrical configuration.

High accuracy codes generally use Monte-Carlo techniques to evolve trajectories of individual particles, for example FREYA [4], NFREYA [5], TRANSP [6], NUBEAM [7], MSESIM [8], BBNBI [9] and FIDASIM [10]. These codes couple the collisionless treatment of the high energy neutrals with collisional models of the beam deposition in the plasma cavity. The most significant issue with these codes is that execution time tends to be long as a large number of particles need to be followed to reduce statistical fluctuations. However, through simplifications in the beam formulation, codes such as PENCIL [11] and SUPERCODE [12] are capable of generating faster approximating solutions. The SINBAD code [13] offers improvements over these earlier first-generation approximate methods. Based on a so-called *narrow beam model* the approach in SINBAD assumes the beam source is planar with a small cross-sectional area compared to the length of the beam-line. Results from SINBAD provide reasonable matches to FREYA, TRANSP and to measured NBI data [13]. The NEMO code [14] is a modernised version of the SINBAD code enabling it to be included in the CRONOS integrated modelling suite [15] and to be used by the European Integrated Tokamak Modelling Task Force (ITM-TF) [16]. The NEBULA code [17] also uses the *narrow beam model*

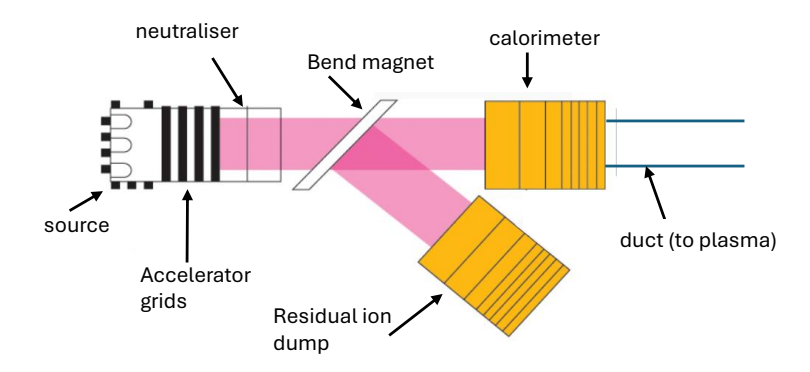


Figure 1. Schematic of the neutral beam system on MAST Upgrade illustrating the salient features of a generic system. (figure is based on [20]).

proposed by SINBAD. A similar but not identical approach has been recently described by Bannmann *et al.* [18, 19] to model neutral beam injection and halo formation using a set of Gaussian pencil (Gausscil) beams, formed by dividing the source grid into a set of rectangular areas. The results of the model are shown to be in good agreement with FIDASIM.

Whilst earlier approaches (for example PENCIL) treated the beam as a single entity, later models provided the capability of sub-dividing the beam and summing the contributions; it was found that the number of subdivided beams required is less than the total number of PINI beamlets and as low as 2x5 [18] which is an advantage for computational speed. The main hypothesis for the application of these simplified approaches is that the plasma conditions are sufficiently homogeneous across the constituent beamlets in planes parallel to the beam source; this sets a condition on the minimum number of beamlets and ultimately limits the applicability for using a non Monte-Carlo method.

Figure 1 shows a schematic of the beam system on MAST Upgrade. The first stage is the generation of ions. These are subsequently accelerated, shaped and focussed via an electric field generated by a cascade of grids held at fixed potentials. The final grid is at *tokamak* (*or device*) earth potential and particles emerge into a neutralisation chamber. Following this, remaining ions are diverted off to a beam dump with an applied magnetic field, whilst the neutral particles stream down a duct into the plasma (tokamak or stellarator) cavity. During the final transit a proportion of the neutral particles may be reionised due to interactions with the background neutral gas. Furthermore, the presence of baffles or other fixed components may scrape off part of the streaming neutral particle beam; these are collectively referred to as *transmission losses*.

The usual approach for computing the neutral beam distribution arriving into the plasma cavity is to start with the flux of fast ions exiting the final earthed acceleration grid into the neutraliser chamber. The salient features relevant for determining the downstream beam distribution are as follows:

- 1. The velocity distribution of the neutralised ions in the neutraliser chamber matches the distribution of the source ions exiting the final accelerator grid. Evidence to support this is contained in a recently published computational model for space charge neutralisation of positive ion beams, Holmes and McAdams [21] who show that for a Deuterium beam of 120 kV, 60 A the role of space charge forces is inconsequential in the beam transport at least until the bend magnet is reached. Similar evidence is available for ITER negative ion beams from simulations using the OPERA code [22].
- 2. The neutraliser efficiency is known. The overall neutraliser efficiency is generally obtained by a combination of measurements taken within the beamline during dedicated calibration exercises and simulation [23, 24, 25]. Typical values on JET for deuterium injection range from 30-60% depending on precise details of beam species mix produced by the ion source and acceleration voltage.
- 3. The transmission factor is known. The beam transmission factor accounts for "baffle losses": particles lost by interactions with structures at the edge of the beam. The transmission factor cannot be obtained by direct measurement and thus is estimated. On JET, this is achieved by combining neutral beam test bed data with ray tracing simulations giving a value of 75% [25]. This factor therefore accounts for one of the largest uncertainties

in the overall beam power delivered to the plasma which, combined with other uncertainties results in a total uncertainty of 10% in power delivered to JET. The PINI simulator code [26] takes full account of baffle losses as do other codes, for example BBNBI which has been used to model JET and AUG tokamaks [9]. Another factor included in the PINI simulator code is transmission losses due to reionisation of the beam with the background gas in the duct between the neutraliser chamber and the tokamak plasma cavity.

4. Spatial variations in the beam flux and velocity divergence on the beam source grid are known. For the JET Positive Ion Neutral Injector (PINI) ion source design, detailed measurements of the ion-source non-uniformity were made on the NB test-bed(NBTB) [27, 28, 29, 30]. Measurements of the beam profile with high spatial resolution and accurate electrical measurements at the PINI accelerator grids were then combined with detailed modelling to infer the beam divergence characteristics. For each JET PINI, following initial construction and again after any significant engineering work on the PINI, a detailed characterisation exercise was executed on the NBTB recording the beam profile over a wide range of voltages and perveance values. (These characterisations are kept as internal reports and are not generally available to the public). Lacking dedicated test-bed measurements as is the case for JET PINIs, the MAST Upgrade beams rely on the fact that the construction of the PINIs themselves are very similar to the JET PINIs.

In this paper we describe a new analytical approach to calculate the propagation of a probability density function (PDF) of collisionless neutral particles with a Maxwellian velocity distribution and arbitrary spatial distribution emitted from a surface towards a fixed focus. In comparison with previous approaches based on the narrow beam model of SINBAD or the Gaussian pencil beams of Bannmann, the methodology presented in this paper is mathematically rigorous relating the PDF at the source with the PDF at any point beyond the source. This is achieved by a change of variables enabling a 1:1 mapping of particles between the source and points beyond. The model takes into account transmission losses, expressed as a truncation in the velocity component of the PDF. An outcome of the model is that the PDF at any point both on the source or elsewhere can be expressed as the product of two PDFs for the spatial and velocity distributions. Furthermore, contrary to the assumption of constant velocity variance employed in other simplified models, the velocity variance changes with distance from the source.

Section 2 considers the case of a spatially truncated 1-D source with normal distribution, and with a normally distributed angular velocity (pitch). Expressions for the full distribution at a fixed normal distance from the source are expressed as the product of two constituent distributions in pitch and in spatial position. Sections 3 compares results from the new analytic model with the model used in [18] and from 1-D ray-tracing calculations. Section 4 includes the effects of baffle losses on the particle distribution and obtains the transmission factor. Section 5 considers non-Gaussian source distributions. This is accomplished by expressing the distribution in terms of a set of overlapping Gaussian distributions whose magnitude are computed such that on aggregate they match the source distribution. Section 6 extends the model to a 2-D source distribution. Finally section 7 presents results of the model applied to the MAST Upgrade tokamak.

2. 1-D source distribution

This section derives an analytical expression for the particle distribution at an arbitrary point ahead of a distributed particle source. Figure 2 illustrates the geometry, aligned with the right-handed Cartesian coordinates u,v,w and unit vectors $\underline{\hat{u}}$, $\underline{\hat{v}}$, $\underline{\hat{w}}$. The particle source lies on the vertical line through points O and O extending from O and O and O and is directed towards a focal point O and O are represents the locus of peak density. While most of the beam is constrained within the dashed lines, velocity divergence causes some particles to deviate beyond these boundaries. Point O is situated on line O and arriving at O on line O and O on line O on

The positions of points P, Q and F are defined as follows:

$$P = O + p_u \hat{\underline{u}} + p_v \hat{\underline{v}} \tag{1}$$

$$Q = O + q\hat{\underline{v}} \tag{2}$$

$$F = O + f_u \hat{\underline{u}} + f_v \hat{\underline{v}} \tag{3}$$

The PDF of particles at the source based on position q and pitch angle θ is defined as:

Figure 2. Configuration of problem with a 1-D source.

$$g(q,\theta) = \begin{cases} \frac{A}{n_2} \exp\left(-\frac{q^2}{2\sigma^2} - \frac{(\theta - \theta_\mu)^2}{2\delta^2}\right) & \text{if } q_{\min} \le q \le q_{\max} \text{ and } -\frac{\pi}{2} \le \theta \le \frac{\pi}{2} \\ 0 & \text{otherwise} \end{cases}$$
(4)

where θ_{μ} denotes the counter-clockwise angle between the normal to the source $(\hat{\underline{u}})$ and \overline{QF} , while θ is the counter-clockwise angle between $\hat{\underline{u}}$ and \overline{QP} . The normalisation constant A and the terms n_1, n_2 are given by:

$$A = \frac{1}{2\pi\sigma\delta n_1} \tag{5}$$

$$n_1 = \Phi\left(\frac{q_{max}}{\sigma}\right) - \Phi\left(\frac{q_{min}}{\sigma}\right) \tag{6}$$

$$n_2 = \Phi\left(\frac{\pi/2 - \theta_\mu}{\delta}\right) - \Phi\left(\frac{-\pi/2 - \theta_\mu}{\delta}\right) \tag{7}$$

where $\Phi(x)$ is the cumulative distribution function (CDF) of the standard normal distribution:

$$\Phi(x) = \frac{1}{2} \left(1 + \operatorname{erf}(x/\sqrt{2}) \right) \tag{8}$$

with $erf(\cdot)$ denoting the error function.

The PDF $g(q,\theta)$ characterises the source distribution as a spatially truncated normal distribution centred about the point O and truncated normal velocity distribution directed towards focus F. In the next section we derive expressions to map this distribution to the line X-X which is parallel to the source and located a distance p_u from it, i.e. $g(q,\theta) \rightarrow g_{\alpha}(p_v,\theta)$. To facilitate this mapping, we derive expressions relating the coordinates and angles involved. By computing the scalar and cross products of vectors \overline{FQ} and \overline{PQ} with \hat{u} we obtain:

$$\sin \theta = \frac{P - Q}{|PO|} \cdot \hat{\underline{v}} \tag{9}$$

$$\cos\theta = \frac{P - Q}{|PO|} \cdot \hat{\underline{u}} \tag{10}$$

$$\sin \theta_{\mu} = \frac{F - Q}{|FO|} \cdot \hat{\underline{y}} \tag{11}$$

$$\cos \theta_{\mu} = \frac{F - Q}{|FQ|} \cdot \hat{\underline{u}} \tag{12}$$

Combining these relations, we find:

$$(P - Q) \cdot \hat{u} \tan \theta = (P - Q) \cdot \hat{v} \tag{13}$$

$$(F - Q) \cdot \hat{u} \tan \theta_u = (F - Q) \cdot \hat{v} \tag{14}$$

(15)

Substituting equations 1, 2 and 3 for P, Q and F respectively yields:

$$q = -p_u \tan \theta + p_v \tag{16}$$

$$\tan \theta_{\mu} = \frac{f_{\nu} - q}{f_{u}}$$

$$4$$
(17)

In the limit $f_u \gg f_v - q$, the small-angle approximation $\tan \theta_\mu \sim \theta_\mu$ holds. Furthermore equation 4 indicates that significant values of $g(q, \theta, \theta_\mu)$ occur when $(\theta - \theta_\mu)/\delta \sim 1$, implying $\theta \sim \delta + \theta_\mu$ if $\delta \ll 1$. Combining these approximations yields $\tan \theta \sim \theta$. These approximations are satisfied in the JET and ITER neutral beamlines [31, 32]. Under these conditions, equations 16 and 17 simplify to:

$$q = -p_u \theta + p_v \tag{18}$$

$$\theta_{\mu} = \frac{f_{\nu} - q}{f_{\mu}} \tag{19}$$

Rearranging these equations yields:

$$\theta = \frac{p_v - q}{p_u} \tag{20}$$

$$\theta_{\mu} = \frac{p_u \theta - p_v + f_v}{f_u} \tag{21}$$

The following section uses these small-angle approximations as expressed in equations 18 to 21.

2.1. Transformation of PDF

In this section we obtain the mapping $g(q, \theta) \to g_{\alpha}(p_{\nu}, \theta)$, expressed in separable form as the product of two component PDFs:

$$g_{\alpha}(p_{\nu}, \theta; p_{u}) = g_{1}(\theta; p_{u}, p_{\nu})g_{2}(p_{\nu}; p_{u})$$
 (22)

where the notation a,b;c indicates that a PDF is a function of variables $\{a,b\}$ and c is an additional parameter (i.e. $\int g_X(a,b;c)da\ db=1$). Whereas g_α describes the total mapped PDF in an arbitrary position in phase space, the components g_1 and g_2 each express distinct aspects of g_α . The PDF g_1 is the velocity distribution at a single spatial point (p_u,p_v) and the PDF g_2 is the spatial distribution evaluated on the section X-X located at p_u shown in figure 2. Substituting equations 18 and 21 into 4 to eliminate q and θ_μ , the PDF g_α defined in equation 22 can be expressed as:

$$g_{\alpha}(p_{\nu}, \theta; p_{\mu}) = AJ \exp(-a\theta^2 - b\theta - c)$$
 (23)

where

$$a = \frac{p_u^2 f_u^2 \delta^2 + \sigma^2 (f_u - p_u)^2}{2\sigma^2 f_u^2 \delta^2}$$
 (24)

$$b = -\frac{p_u p_v f_u^2 \delta^2 + \sigma^2 (p_u - f_u)(p_v - f_v)}{\sigma^2 f_u^2 \delta^2}$$
 (25)

$$c = \frac{p_v^2 f_u^2 \delta^2 + \sigma^2 (f_v - p_v)^2}{2\sigma^2 f_u^2 \delta^2}$$
 (26)

and

$$J = \begin{vmatrix} \frac{\partial q}{\partial p_{\nu}} \Big|_{\theta} & \frac{\partial q}{\partial \theta} \Big|_{p_{\nu}} \\ \frac{\partial \theta}{\partial p_{\nu}} \Big|_{\theta} & \frac{\partial \theta}{\partial \theta} \Big|_{p} \end{vmatrix} = 1 \tag{27}$$

is the Jacobian determinant accounting for the change of variable from $\{q, \theta\}$ to $\{p_{\nu}, \theta\}$. Completing the square for θ , equation 23 can be written as a product of two PDF functions as shown in equation 22 with

$$g_{1}(\theta; p_{u}, p_{v}) = \begin{cases} \frac{1}{\sqrt{2\pi}\sigma_{*}n_{2}} \exp\left(-\frac{(\theta - \mu_{*})^{2}}{2\sigma_{*}^{2}}\right) & \theta_{min} \leq \theta \leq \theta_{max} \\ 0 & \theta < \theta_{min} \\ 0 & \theta > \theta_{max} \end{cases}$$
(28)

$$g_2(p_v; p_u) = Bn_2(p_u, p_v) \exp\left(-\frac{(p_v - \mu_r)^2}{2\sigma_r^2}\right)$$
(29)

where

$$\mu_*(p_u, p_v) = \frac{-b}{2a} = \frac{hp_v(hp_u - f_u) + hf_v(f_u - p_u)}{k}$$
(30)

$$\sigma_*(p_u)^2 = \frac{1}{2a} = \frac{f_u^2 \delta^2 h}{k}$$
 (31)

$$\mu_r(p_u) = \frac{f_v p_u}{f_u} \tag{32}$$

$$\sigma_r^2(p_u) = \sigma^2 \left(\frac{(hp_u - f_u)^2}{hf_u^2} + \frac{h - 1}{h} \right)$$
 (33)

$$\theta_{\min}(p_u, p_v) = \begin{cases}
\tan^{-1}\left(\frac{p_v - q_{\max}}{p_u}\right), & p_u > 0 \\
-\frac{\pi}{2}, & p_u = 0 \text{ and } q_{\min} < p_v < q_{\max} \\
0 & \text{otherwise}
\end{cases}$$
(34)

$$\theta_{\min}(p_u, p_v) = \begin{cases} \tan^{-1}\left(\frac{p_v - q_{\max}}{p_u}\right), & p_u > 0\\ -\frac{\pi}{2}, & p_u = 0 \text{ and } q_{\min} < p_v < q_{\max}\\ 0 & \text{otherwise} \end{cases}$$

$$\theta_{\max}(p_u, p_v) = \begin{cases} \tan^{-1}\left(\frac{p_v - q_{\min}}{p_u}\right), & p_u > 0\\ +\frac{\pi}{2}, & p_u = 0 \text{ and } q_{\min} < p_v < q_{\max}\\ 0 & \text{otherwise} \end{cases}$$

$$(34)$$

$$n_2(p_u, p_v) = \Phi\left(\frac{\theta_{\text{max}} - \mu_*}{\sigma_*}\right) - \Phi\left(\frac{\theta_{\text{min}} - \mu_*}{\sigma_*}\right)$$
(36)

$$B(p_u) = A\sqrt{2\pi}\sigma_* \tag{37}$$

in which

$$h = 1 + \frac{\delta^2 f_u^2}{\sigma^2} \tag{38}$$

$$k(p_u) = (hp_u - f_u)^2 + (h - 1)f_u^2$$
(39)

In the limits $|p_v - q_{min}| \ll p_u$ and $|p_v - q_{max}| \ll p_u$, equations 34 and 35 become:

$$\theta_{min}(p_u, p_v) \approx \frac{p_v - q_{max}}{p_u} \tag{40}$$

$$\theta_{max}(p_u, p_v) \approx \frac{p_v - q_{min}}{p_u} \tag{41}$$

In this limit, substituting for θ_{min} , θ_{max} , μ_* , the arguments of the $\Phi(\cdot)$ terms appearing in equation 36 are:

$$\frac{\theta_{min} - \mu_*}{\sigma_*} = -\frac{h(f_u p_v + f_v p_u)(f_u - p_u) + kq_{max}}{\sigma_* p_u k}
\frac{\theta_{max} - \mu_*}{\sigma_*} = -\frac{h(f_u p_v + f_v p_u)(f_u - p_u) + kq_{min}}{\sigma_* p_u k}$$
(42)

$$\frac{\theta_{max} - \mu_*}{\sigma_*} = -\frac{h(f_u p_v + f_v p_u)(f_u - p_u) + kq_{min}}{\sigma_* p_u k}$$
(43)

When $p_u = f_u$, these simplify to:

$$\left. \frac{\theta_{\min} - \mu^*}{\sigma_*} \right|_{p_u = f_u} = -\frac{q_{\max}}{\sigma_* p_u} \tag{44}$$

$$\frac{\theta_{min} - \mu^*}{\sigma_*} \bigg|_{p_u = f_u} = -\frac{q_{max}}{\sigma_* p_u}$$

$$\frac{\theta_{max} - \mu_*}{\sigma_*} \bigg|_{p_u = f_u} = -\frac{q_{min}}{\sigma_* p_u}$$
(44)

and n_2 is independent of p_v .

From equations 28 to 45, we observe that by considering a fixed focus (f_u, f_v) :

- 1. $g_1(\theta; p_u, p_v)$ is a truncated normal distribution whereas $g_2(p_v; p_u)$ is a truncated normal distribution at $p_u = 0$ (this is consistent with equation 4) and an unbounded distribution for $p_u > 0$.
- 2. The parameters of the normal distribution $g_1(\theta; p_u, p_v)$ are σ_* , μ_* and n_2 . The parameter n_2 expresses the truncation of the normal distribution; σ_* is independent of both p_v and f_v , whereas for a given value of p_u , μ_* varies linearly with p_v . The characteristics are plotted in figure 3. At specific limits,
 - (a) when $p_u = 0$ (at the source plane), $\mu_* = (f_v p_v)/f_u$, $\sigma_* = \delta$ (i.e. δ is consistent with equation 4).
 - (b) when $p_u = f_u$ (at the focal plane), $\mu_* = p_v/f_u$, $\sigma_* = \sigma/f_u$. (i.e. at longer focal distances the beam becomes more collimated and with a reduced standard deviation in velocity.)
 - (c) when $p_u = f_u/h$, $\mu_* = f_v/f_u$, i.e. μ_* is independent of p_v ; and $\sigma_* = \sqrt{\delta^2 + (\sigma/f_u)^2}$, increasing from $\sigma_* = \delta$ at $p_u = 0$, and thereafter decreasing with $\sigma_* = 0$ as $p_u \to \infty$.
 - (d) in the limit $p_u/f_u \to \infty$, $\mu_* = p_v(1 f_v)$ and $\sigma_* = 0$ i.e. at distances well beyond the focus, the mean velocity direction varies linearly with p_v and its variance is zero.
 - (e) in the limit $f_u/p_u \to \infty$, $\mu_* = p_v(hf_v 1)$ and $\sigma_* = \delta$ i.e. as the focal point moves towards ∞ at finite distances from the source the mean velocity direction varies linearly and its variance is δ^2 .
- 3. The parameters of $g_2(p_v; p_u)$ are B, n_2 , μ_r and σ_r . The parameter B is a normalising factor to ensure that $\int g_2(p_v; p_u) dp_v = 1$. Figure 4(a) plots the variation of n_2 ; at $p_u = f_u$ the variation in n_2 with respect to p_v reduces to zero and $g_2(p_v; p_u)$ is a normal distribution. Figure 4(b) plots the variation of σ_r . Although $g_2(p_v; p_u)$ is not in general a Gaussian distribution, σ_r provides an approximation to the standard deviation fit to a normal distribution.

At specific limits,

- (a) when $p_u = 0$ (at the source plane), $\mu_r = 0$, $\sigma_r = \sigma$ (i.e. σ_r is consistent with equation 4).
- (b) when $p_u = f_u$ (at the focal plane), $\mu_r = f_v$, and $\sigma_r = \delta f_u$. In the limit $|p_v q_{min}| \ll p_u$ and $|p_v q_{max}| \ll p_u$, $g_2(p_v; p_u)$ is a truncated Gaussian.
- (c) when $p_u = f_u/h$, $\sigma_r^2 = h\sigma^2/f_u^2$, $\mu_r = f_v$.
- (d) in the limit $p_u/f_u \to \infty$, $\sigma_r = \infty$ and
 - if $f_v = 0$ then $\mu_r = 0$
 - if $f_v > 0$ then $\mu_r = +\infty$
 - if $f_v < 0$ then $\mu_r = -\infty$

i.e. at distances well beyond the focus, the radial variance tends to ∞ whereas its mean value dependence on whether f_v is non-zero, and also its sign if non-zero.

- (e) in the limit $f_u/p_u \to \infty$, $\mu_r = 0$ and $\sigma_r = \sigma$ i.e. as the focal point moves towards ∞ at finite distances from the source the radial variance tends to σ and its mean velocity is zero.
- 4. The p_u -value where σ_r and σ_* reach their extreme points and where μ_* is independent of p_v are all coincident at $p_u = f_u/h$. Since in general h > 1 (see equation 38) this position always lies between the beam source ($p_u = 0$) and the focal plane ($p_u = f_u$).

3. Model validation

In this section we compare the results of the 1-D model described in section 2 with a 1-D ray-tracing model and with the Bannmann model for a single Gausscil Beam. The parameters are based on the neutral beam assembly installed on MAST Upgrade [32] that has a beam half-width=82.5mm, focus = 12m, and beam divergence of 0.6 degrees. The line joining the mid-point of the source and focal point is taken to be perpendicular to the source. Specific details of the models are as follows:

Monte-Carlo Model

For the purpose of validating the model described in section 2, a 1-D ray tracing code was written in Python. The geometry is as shown in figure 2. A set of rays $(n = 10^8)$, spatially distributed according to a truncated normal distribution about q = 0 with standard deviation 82.5mm were launched from the source within the range $q_{min} < q < q_{max}$. The orientation of each ray emanating from a given point was sampled from a normal distribution with a mean orientation directed towards the focal point and with angular standard deviation 0.6 degrees. The rays were projected a distance u from the source, and results presented as histograms.

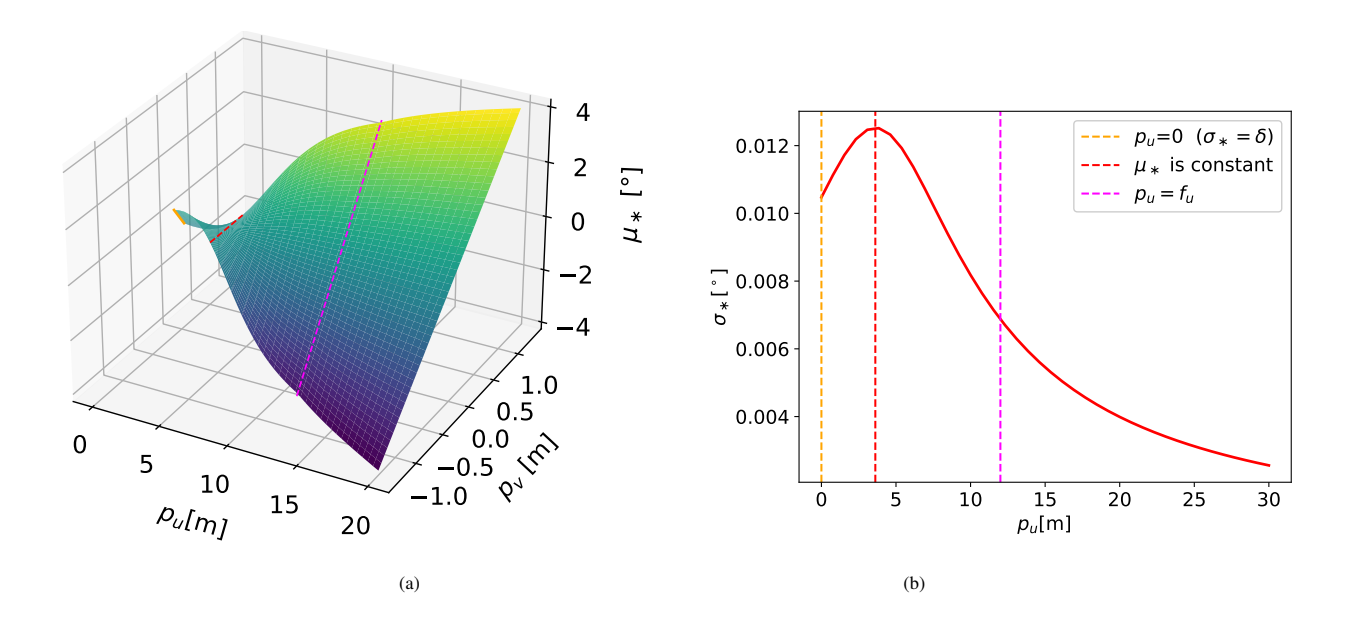


Figure 3. (a) Variation of μ_* with p_u and p_v . (b) Variation of σ_* with p_u . The lines shown are at $p_u=0$ (orange line) and $p_u=f_u$ (magenta line). The red line is at the value of p_u where μ_* is independent of p_v , σ_* reaches its maximum value and σ_r (see figure 4b) reaches it minimum value. (Beam parameters are $\sigma=82.5$ mm, $\delta=0.6$ degrees, O=(0,0), F=(12m,0), $q_{min}=-\sigma$, $q_{max}=+\sigma$)

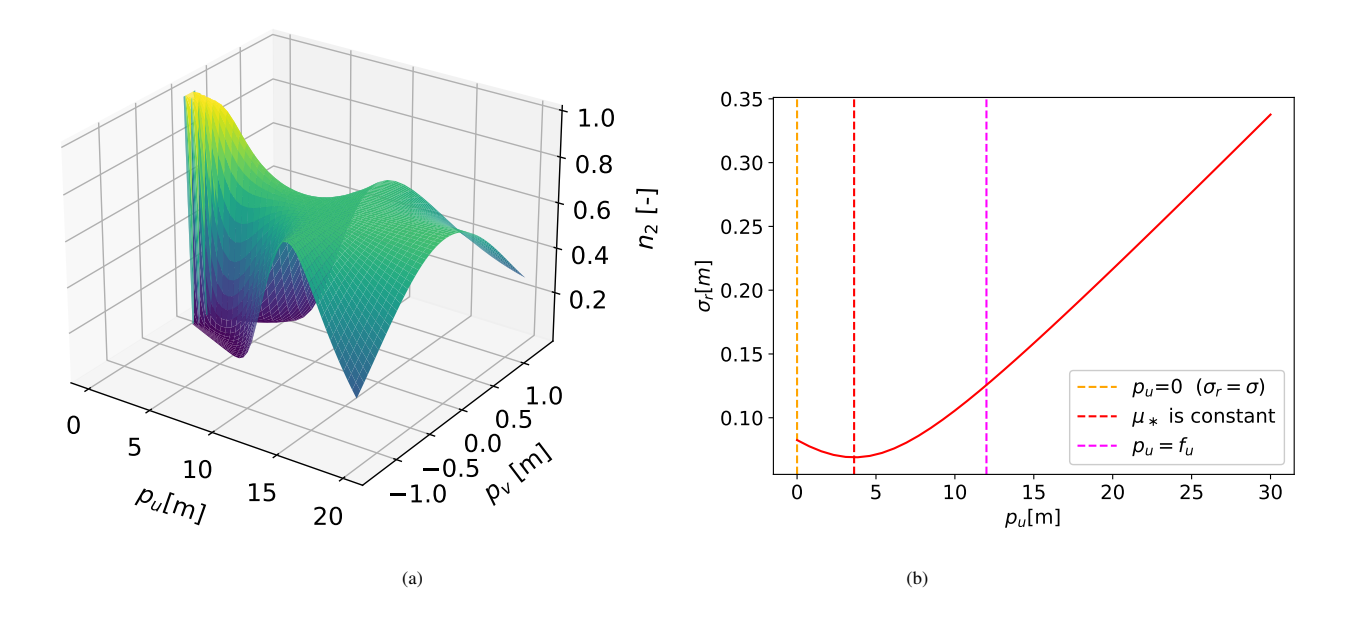


Figure 4. (a) Variation of n_2 with p_u and p_v . (b) Variation of σ_r with p_u . The lines shown are at $p_u = 0$ (orange line) and $p_u = f_u$ (magenta line). The red line is at the value of p_u where both μ_* is constant and σ_* reaches its minimum value. (Beam parameters are $\sigma = 82.5$ mm, $\delta = 0.6$ degrees, O = (0,0), F = (12m,0), $q_{min} = -\sigma$, $q_{max} = +\sigma$)

Figure 5. Geometrical depiction of a single Gausscil beam $(\gamma > \delta)$ [18].

Bannmann Model

The Bannmann model represents the beam source by a set of Gausscil beams. Figure 5 illustrates a single Gausscil for the case $\delta < \gamma$ on orthogonal axes uv. The geometrical details are taken from its implementation in the Minerva Bayesian framework [33]. The beam source, located at u = 0 on the left side of the figure, follows a normal distribution $\mathcal{N}(0,\sigma^2)$ about the point O=(0,0) with $\sigma=w/2=82.5$ mm, truncated at $v=\pm\sigma$. Particles are emitted from all points at the source in the positive u-direction towards the focus F with a divergence angle δ . The solid lines in the figure show the trajectory of two particles launched with zero divergence from the extreme edges of the source converging at the focal point $F = (f_u, 0)$. Neglecting velocity divergence, all particles would converge at F. However, velocity divergence causes the majority of particles launched at the source to miss F. To account for this, the model introduces an ad hoc assumption: particles pass through one of two "virtual" focal points, depending on their observed position. These virtual focal points, $F_f = (f_f, 0)$ and $F_b = (f_b, 0)$, are defined by the trajectories of particles emitted from the source's edges at an angle δ relative to the optimum focus angle γ shown by the dashed lines in the figure. Particles in front of $F(u \ge f_u)$ are focused at F_f , while those behind $F(u < f_u)$ are focused at F_b . Although this ad hoc approach provides a practical framework for modeling, it may not accurately reflect the physical trajectories of particles emitted from the source.

Expressions for the geometrical angles ϕ , ξ ; focal positions f_f and f_b , and beam width (standard deviation) σ_f at a point $P = (p_u, p_v)$ are:

$$\gamma = \tan^{-1} \frac{\sigma}{f_u}$$

$$\xi = \gamma + \delta$$
(46)

$$\xi = \gamma + \delta \tag{47}$$

$$\phi = |\gamma - \delta| \tag{48}$$

$$f_f = \frac{\sigma}{\tan \xi} \tag{49}$$

$$f_b = \frac{\sigma}{\tan(\gamma - \delta)} \tag{50}$$

$$\sigma_f = \begin{cases} |f_b - p_u| \tan \phi, & p_u < f_u \\ |p_u - f_f| \tan \xi, & p_u > f_u \\ f_u \tan(\gamma + \delta) - \sigma, & p_u = f_u \end{cases}$$

$$(51)$$

In the limit, $f_u \gg \sigma$ and $\delta \ll 1$

$$\gamma = \frac{\sigma}{f_u} \tag{52}$$

$$f_f = \frac{\sigma}{\gamma + \delta} \tag{53}$$

$$\gamma = \frac{\sigma}{f_u} \tag{52}$$

$$f_f = \frac{\sigma}{\gamma + \delta} \tag{53}$$

$$f_b = \frac{\sigma}{\gamma - \delta} \tag{54}$$

$$\sigma_f = f_u \delta \qquad (p_u = f_u) \tag{55}$$

$$\sigma_f = f_u \delta \qquad (p_u = f_u) \tag{55}$$

Figure 6. Geometrical depiction of a single Gausscil beam $(\delta > \gamma)$ [18].

The velocity is taken to be normally distributed $\mathcal{N}(\theta_u^b(p_u, p_v), \delta^2)$ where:

$$\theta_{\mu}^{b}(p_{u}, p_{v}) = \begin{cases} \tan^{-1}\left(\frac{-p_{v}}{f_{b} - p_{u}}\right), & p_{u} < f \\ \tan^{-1}\left(\frac{p_{v}}{p_{u} - f_{f}}\right), & p_{u} \ge f \end{cases}$$
(56)

In the case $\delta > \gamma$, $f_b < 0$ and the beam model is modified as shown in figure 6. In this case the beam divergence dominates the focusing of the beam even in the near-focus region $u < f_u$. Equations 46 to 56 remain valid. In the MAST Upgrade case, $f_u = 12m$, w/2 = 82.5mm, $\delta = 0.6$ degrees yielding $\gamma = 0.39$ degrees. Therefore we are in the regime $\delta > \gamma$ and the results presented use the model shown in figure 6.

In both the Bannmann model and the analytic model presented in Section 2, the velocity is normally distributed, though in the latter case it has truncated bounds. In the Bannmann model, the mean velocity depends on one of two virtual focal positions (see equations 56) and the standard deviation is constant. In contrast, the analytic model has a single focal point and a position-dependent standard deviation of velocity (c.f. $\sigma_{\star}(p_u)$ in equation 31).

3.1. Results

Figure 7 plots the spatial variation at six discrete values of p_u . From inspection of the figure:

- 1. The agreement between the analytic model and the ray-tracing model is excellent for all values of p_u . The distribution is not a normal apart from at the positions p_u and $p_u = f$.
- 2. At $p_u = 0$ (the source location) the distribution for all three cases is a truncated normal distribution in agreement with the requirements of the model.
- 3. At $p_u = 12m$ (the "focal-plane") the Bannmann model is in agreement with the analytic model and ray tracing model. This is the case because $f_u \gg \sigma$ and $\delta \ll 1$ and equation 55 applies i.e. $\sigma \approx f_u \delta$, the value for the analytic model (see section 2.1, observation 3(b)).
- 4. The Bannmann model does not agree perfectly with the analytic model and ray-tracing results away from $p_u = 0$ and $p_u = f$.

Figure 8 plots the velocity distribution at $p_v = 0$, $p_v = \sigma_r$ and $p_v = 2\sigma_r$ at three positions along the beam: $p_u = 0$, $p_u = 12m$, and $p_u = 20m$. There is no plot at $p_u = 0$, $p_v = 2\sigma$ as the beam is truncated spatially at $p_v = \sigma$. From inspection of the figure and the model equations:

- 1. The agreement between the analytic model and the ray-tracing model is excellent for all cases. This includes the details of the truncation limits.
- 2. The Bannmann model agrees with the ray-tracing model and analytic model only at the mid-point of the source (see the left-hand graph in figure 8(a)). The use of a virtual focus position (F_b) rather than the true focal position (F) explains the discrepancy in the right plot of figure 8(a). The assumption that the velocity standard deviation is δ , independent of position, yields values that are at too large at $p_u = 12m$ and $p_u = 20m$. Finally the Bannmann model assumes the distributions are unbounded in comparison with the analytic model that provides truncation bounds for $p_u > 0$.

In conclusion, agreement between the analytic model and ray-tracing model is excellent in all cases. The reason that the Bannmann model works well for interpretation of Charge Exchange Recombination Spectroscopy (CXRS) data [19] is explained by the fact that the details of the velocity distribution are not important in this case.

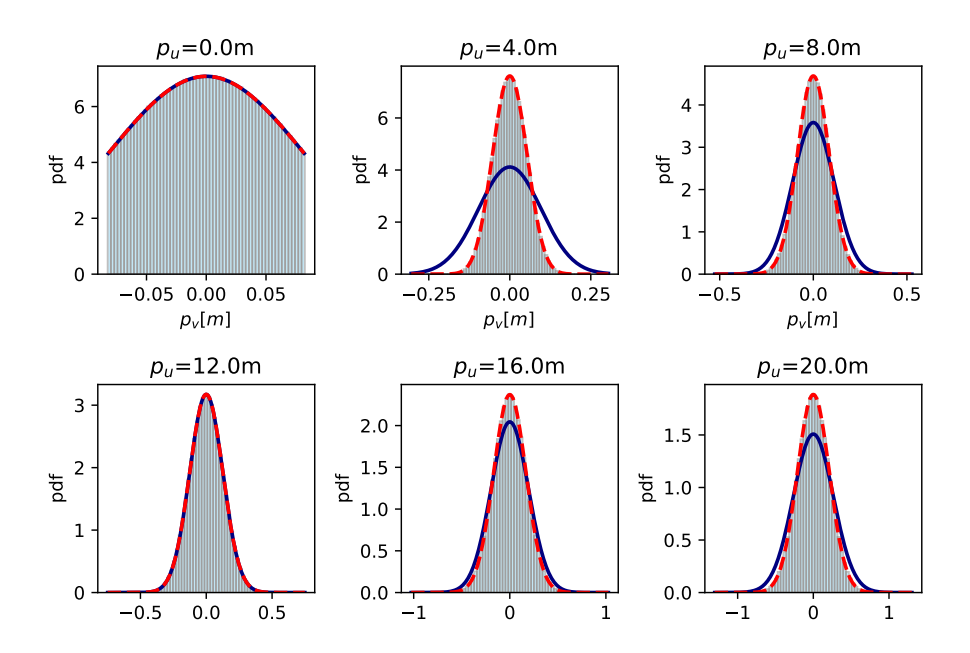


Figure 7. Comparison of $g_2(p_v; p_u)$ (red line) with ray tracing calculation (histogram) and the Bannmann [18] model (blue line). The results are shown for six p_u values; $p_u = 0$ is the source location, $p_u = 12m$ is the focal plane.

4. Transmission losses

Transmission losses in neutral beamlines occur when obstructions, such as baffles, intercept portions of the beam, effectively "scraping" off its edges. For a point P downstream of an obstruction at coordinates $B = (b_u, b_v)$ (refer to figure 9), the obstruction angle θ_b is defined as:

$$\theta_b = \tan^{-1} \left(\frac{p_v - b_v}{p_u - b_u} \right) \tag{57}$$

Obstructions intercepting the top of the beam are denoted as θ_b^t and those intercepting the bottom as θ_b^b . The sets of these obstructions downstream of point P are $\theta_b^t = \{\theta_{b_1}^t, \dots, \theta_{n_t}^t\}$ and $\theta_b^b = \{\theta_{b_1}^b, \dots, \theta_{n_b}^b\}$, respectively. Equations 34 and 35 impose constraints on the permissible angles:

$$\theta_{\min} < \theta < \theta_{\max}$$
 (58)

The presence of obstructions introduces an additional constraint:

$$\max(\boldsymbol{\theta}_b^t) < \theta < \min(\boldsymbol{\theta}_b^b) \tag{59}$$

Combining these inequalities results in:

$$\max(\boldsymbol{\theta}_b^t, \theta_{\min}) < \theta < \min(\boldsymbol{\theta}_b^b, \theta_{\max})$$
 (60)

This combined constraint ensures that only beam trajectories unobstructed by baffles contribute to the transmission at point P. Taking account of transmission losses simply requires to update the values of θ_{\min} and θ_{\max} in equations 34 and 35 with these new limits (i.e. $\theta_{\min} \to \max(\theta_b^t, \theta_{\min})$ and $\theta_{\max} \to \min(\theta_b^t, \theta_{\max})$). Equations 40 and 41 are transformed in a similar manner.

Reducing the permissible pitch angles affects both the velocity and radial distribution functions, $g_1(\theta; p_u, p_v)$ and $g_2(p_v; p_u)$, respectively, through the term n_2 (equation 36). The modified PDF $g_1(\theta; p_u, p_v)$ retains the property

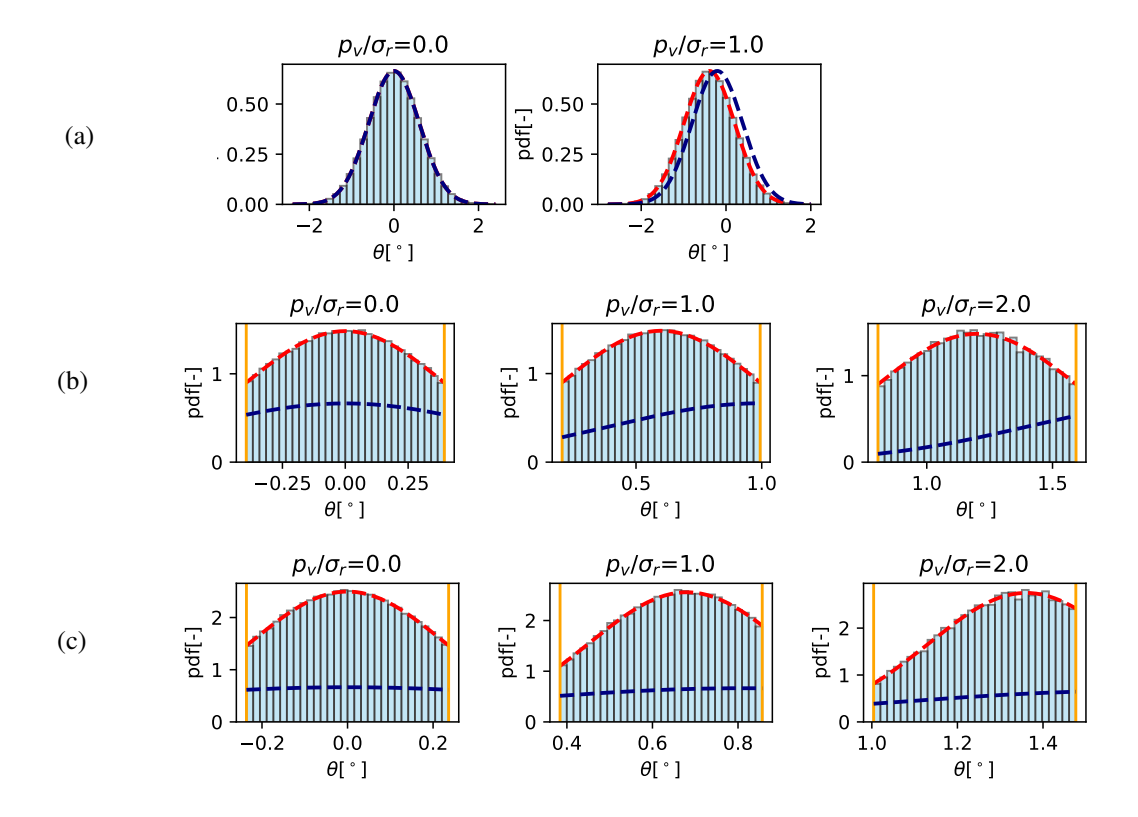


Figure 8. Comparison of $g_1(\theta, p_v; p_u)$ (red dashed line with the truncation limits shown in orange); ray tracing calculation (histogram); and Bannmann [18] model (blue dashed line). Results are shown for: (a) $p_u = 0$, the source location; (b) $p_u = 12m$, (plane through focal point); (c) $p_u = 20m$.

Figure 9. Configuration of problem showing addition of a single baffle point \underline{B} .

 $\int g_1(\theta; p_u, p_v) d\theta = 1$. However the integral of $g_2(p_v; p_u)$:

$$\eta = \int g_2(p_v; p_u) dp_v \tag{61}$$

represents the transmission efficiency; a value of $\eta < 1$ indicates that some particles have been intercepted by obstructions before reaching $u = p_u$. Evaluating η typically involves numerical integration. Since the integral is one-dimensional over a smooth function, it is readily evaluated using Gaussian quadrature.

Figure 10 illustrates the variation in η for a single obstruction located at u = 6m, where the beam is intercepted from above $(v > b_v)$. The figure shows that for values of p_u downstream of the obstruction, η varies between 50% and 100%, depending on the value of b_v . Upstream of the obstruction, η remains constant at 100%.

5. Non-Gaussian 1-D source distributions

In this section, we generalize the spatially truncated normal distribution assumption at the source to accommodate "arbitrary" distributions. This is accomplished by representing the source distribution as a set of spatially distributed truncated Gaussian basis functions.

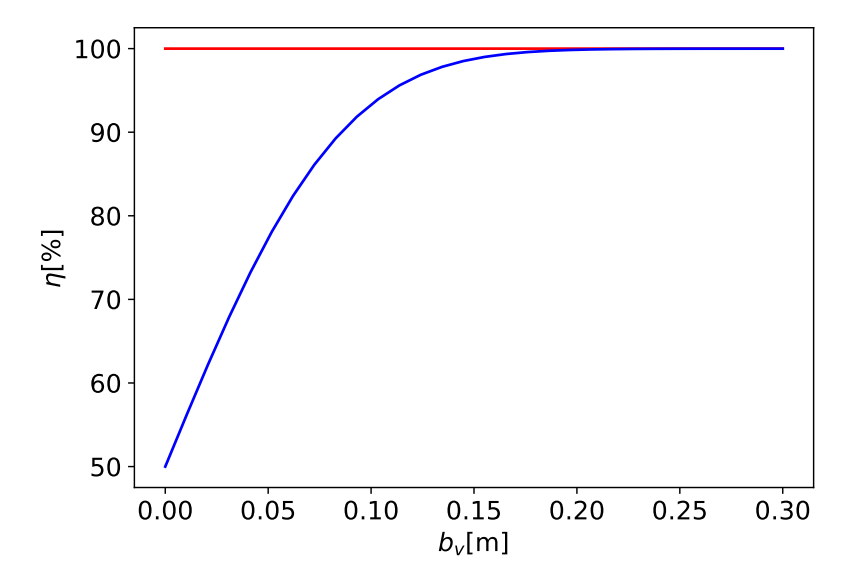


Figure 10. Transmission efficiency for MAST Upgrade case with an obstruction at u = 6m, descending into the beam in the range $0 < b_v < 0.3m$. The red line is for p_u at 0m and 4m; the blue line is for p_u at 8m, 12m and 20m

The PDF, $\Gamma(q, \theta)$, constructed from a collection of n_b normally distributed sources with truncated bounds, is expressed as:

$$\Gamma(q,\theta) = \sum_{k=1}^{n_b} \Gamma_k g_k(q,\theta)$$
 (62)

where $g_k(q,\theta)$ represents the PDF of a single Gaussian source with spatial truncation (c.f. equation 4):

$$g_k(q,\theta) = \begin{cases} \frac{A_k}{n_{2_k}} \exp\left(-\frac{(q-q_k)^2}{2\sigma_k^2} - \frac{(\theta-\theta_\mu)^2}{2\delta^2}\right) & \text{if } q_{min} \le q \le q_{max} \text{ and } -\frac{\pi}{2} \le \theta \le \frac{\pi}{2} \\ 0 & \text{otherwise} \end{cases}$$

$$(63)$$

Here the normalisation constant A_k and the terms n_{1_k} , n_{2_k} , are defined as:

$$A_k = \frac{1}{2\pi\sigma_k\delta n_{1_k}} \tag{64}$$

$$n_{1_k} = \Phi\left(\frac{q_{max}}{\sigma_k}\right) - \Phi\left(\frac{q_{min}}{\sigma_k}\right) \tag{65}$$

$$n_{2_k} = \Phi\left(\frac{\pi/2 - \theta_{\mu_k}}{\delta}\right) - \Phi\left(\frac{-\pi/2 - \theta_{\mu_k}}{\delta}\right) \tag{66}$$

For each $g_k(q, \theta)$, the expressions for the PDFs $g_1(\theta; p_u, p_v)$ and $g_2(p_v; p_u)$ are given by equations 23 to 45 with the transformation $p_v \to p_v - q_k$.

For $\Gamma(q,\theta)$ to be a probability requires that $\sum_{k=1}^{n_b} \Gamma_k = 1$. With this condition satisfied, Γ_k is the fractional flux carried by the k^{th} basis function.

To set about defining parameters of the constituent basis functions to fit a given distribution, we integrate equation 62 over θ :

$$\Gamma^{r}(q) = \sum_{k=1}^{n_b} \Gamma_k g_k^{r}(q) \tag{67}$$

where the marginal distribution $g_k^r(q)$ is:

$$g_k^r(q) = \begin{cases} \sqrt{2\pi} A_k \delta \exp\left(-\frac{(q-q_k)^2}{2\sigma_k^2}\right) & q_{min} \le q \le q_{max} \\ 0 & \text{otherwise} \end{cases}$$
 (68)

With defined q_k and σ_k values, the set of coefficients $\Gamma_b = \{\Gamma_1, \dots, \Gamma_{n_b}\}$ can be determined in a least-squares sense by solving a set of linear equation, with the stiffness matrix composed of $g_k^r(q_i)$ terms evaluated at a set of n_s sample points $q_i \in \{q_1, \dots, q_{n_s}\}$ distributed over the one-dimensional source domain:

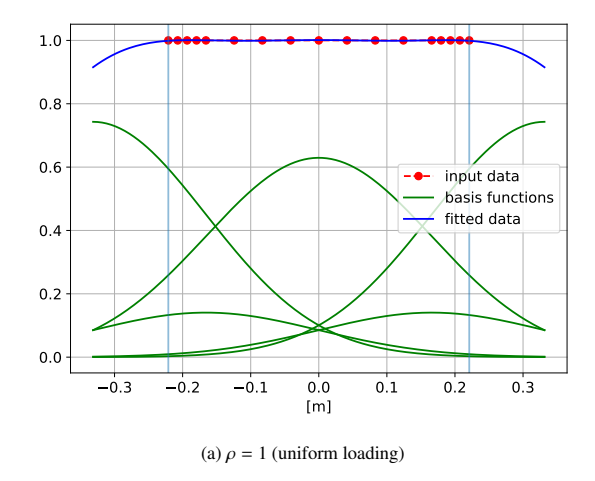
$$\begin{bmatrix} g_1^r(q_1) & \cdots & g_{n_b}^r(q_1) \\ \vdots & \ddots & \vdots \\ g_1^r(q_{n_s}) & \cdots & g_{n_b}^r(q_{n_s}) \end{bmatrix} \begin{bmatrix} \Gamma_1 \\ \vdots \\ \Gamma_{n_b} \end{bmatrix} = \begin{bmatrix} \Gamma^r(q_1) \\ \vdots \\ \Gamma^r(q_{n_s}) \end{bmatrix}$$

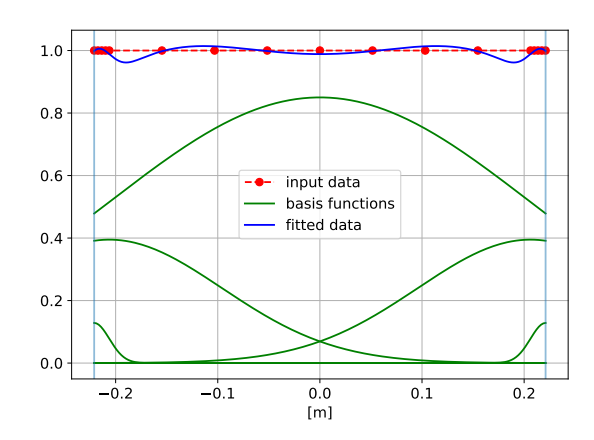
$$(69)$$

Selecting appropriate values for q_k and σ_k is crucial for achieving a smooth fit across the data range, minimizing artefacts such as ringing, especially at the boundaries, and ensuring that all basis function amplitudes are positive (i.e. $\Gamma_i > 0, \forall i \in \{1, 2, ..., n_b\}$). In addition as discussed in section 7 the choice of basis function affects the calculation accuracy of the transmission efficiency.

A single parameter, ρ , controls the 1-D spatial density of the basis functions via a power-law distribution, q^{ρ} . Here, $\rho=1$ corresponds to a uniform distribution, $\rho>1$ increases density toward the beam center, and $\rho<1$ increases density toward the periphery. To mitigate ringing effects, the number of constraint points is increased proportionally to the basis function density. The standard deviation of each basis function is set equal to the distance to its nearest neighbour (or the average distance, in cases of non-uniform distribution) further enhances the fit.

Numerical tests demonstrate that for $\rho > 0.1$ excellent fits are obtained to a set of constant values, $\Gamma'(q_i) = 1$ with $q_{min} \le q_i \le q_{max}$ by placing the mean positions of basis functions within a spatial range extending one standard deviation beyond the physical extent of the beam source. A particular example with $\rho = 1$ is shown in Figure 11(a). All observed computed fits have no ringing and with basis function amplitudes that are always positive. Obtaining good fits with $\rho = 0.1$ is more challenging, because of the reduced density of basis functions in the domain interior. Figure 11(b) shows a typical case for $\rho = 0.1$ and was obtained with the mean positions of basis functions restricted to lie within the range of the source domain. Compared to the previous case, ringing is apparent in the domain interior. Other tests have negative amplitudes for basis functions with means close to the domain boundaries. This is strictly permissible numerically and is not inconsistent physically as the sum of the basis functions is nevertheless greater than zero at all values of q.





(b) $\rho = 0.5$ (high density of basis functions at boundaries).

Figure 11. Results of fitting a set of data with 5 basis functions. The blue curve represents the sum of the constituent basis functions, which are individually shown in green. The boundary of the region, indicated by faint blue vertical lines, is located at ± 0.21 m.

6. Extension to 2-D source distributions

The model can be extended to two dimensions if the beam can be approximated as rectangular and is uncorrelated across dimensions. For cases involving multiple beams (e.g., beamlets within a larger beam), the constraints apply individually to each beamlet rather than to the composite beam. The PDF at the source grid can then be expressed as the product of two independent distributions:

$$g(q_{uv}, \theta_{uv}, q_{wu}, \theta_{wu}) = g_{uv}(q_{uv}, \theta_{uv})g_{wu}(q_{wu}, \theta_{wu})$$
(70)

Here g_{uv} and g_{wu} corresponds to $g(q,\theta)$ as defined in equation 4. The function $g(q_{wu},\theta_{wu})$ is obtained by transforming $g(q,\theta)$ with the substitutions $w \to -v$ and $\theta_{wu} \to -\theta$.

An additional condition is that the baffle edges must align with the beam-aligned uvw coordinate system. However, this is not achievable for circular baffles and may only be partially true for other baffles shapes. Accurate modelling of baffle losses necessitates precise boundary representation, considering combinations of rectangular and circular baffles, as illustrated in figure A.20.

To address this challenge, the source distribution can be decomposed into Gaussian basis functions each occupying a smaller spatial extent, as outlined in Section 5. Figure 12 shows the arrangement of Gaussian basis functions over a two-dimensional source grid, uniformly distributed on a grid, aligned with the coordinate axes. Defining the source intensity distribution as the product of two one-dimensional functions:

$$\Gamma^{r}(v, w) = \Gamma^{r}_{v}(v)\Gamma^{r}_{v}(w) \tag{71}$$

permits the node intensities to be computed in one dimension by solving equations 69 separately for each axis using $\Gamma^r(q_i)$ sets generated from the functions $\Gamma^r_v(v)$ and $\Gamma^r_w(w)$. From these results, the two-dimensional PDF can be assembled.

The independence of the distributions in the uv, and vw planes allows the transmission coefficient, η , to be computed as a sum of products of integrals over n_b basis functions:

$$\eta = \sum_{k=1}^{n_b} \Gamma_k \int (g_{uv})_2^k \, \mathrm{d}v \int (g_{wu})_2^k \, \mathrm{d}w$$
 (72)

Here, $(g_{uv})_2^k$ denotes the k^{th} basis function's g_2 PDF (equation 29) in the uv plane, and $(g_{wu})_2^k$ represents the k^{th} basis function's g_2 PDF in the wu plane.

The next section will explore how the selection of the number of basis function and their spatial distribution influences the model's capacity to accurately account for baffle-induced losses.

7. Application to MAST Upgrade

A new module has been developed within Minerva to model collisionless beam propagation from a two-dimensional beam source comprising multiple sub-beamlets, incorporating realistic baffle geometries. This enhancement leverages Minerva's recent integration with the ITER Integrated Modelling & Analysis Suite (IMAS) [34, 35], enabling the simulation of any neutral beam system for which an appropriate IMAS database instance is available. In this section, we present model predictions for the MAST Upgrade neutral beam system.

The MAST neutral beam system is detailed in Barrett [36], with additional engineering specifications provided in a technical note [32]. As the latter information is not publicly available, we include pertinent details here, along with descriptions of baffles and PINI geometry in the appendix.

The IMAS dataset for the MAST Upgrade beam system specifies the locations of 262 beamlets and their fractional powers; in the data set used for this work there is equal power distribution among all beamlets. The numerical model computes the PDF of the beam by summing the contributions from each beamlet. To reduce computational demands, the model also allows for fitting the spatial variation of fractional powers with a reduced set of basis functions, as described in Section 5. Below, we present results using both the full set of 262 beamlets (*method 0*) and the reduced set of basis functions (*method 1*).

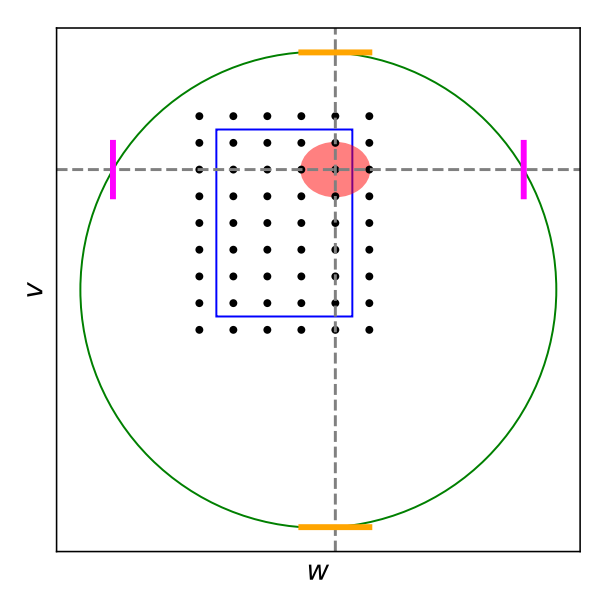


Figure 12. Cartoon of a 2-D beam source, indicating the locations of Gaussian basis functions. The shaded region indicates the range to within one standard deviation for a single Gaussian basis function. The green circle indicates the position of a circular baffle surface, and the magenta and orange lines indicate the positions of effective baffles necessary to compute the 1-D beam propagation in the v-u and w-u planes respectively.

Figure 13 displays contours of PDF variation, marginalized over velocity, for a MAST Upgrade neutral beam using $method\ 0$. The plots are on planes parallel to the beam source, with u denoting the normal distance from the source. Figures are shown at the beam source (u=0m), at two positions downstream toward the plasma cavity (u=1.5m and u=2.5m), and within the plasma cavity (u=7m). The coordinates v and w represent vertical and horizontal positions relative to the center of the beam source.

In figure 13(a), the localized intensity of the 262 beamlets is evident, exhibiting symmetrical mirroring across the beam source. The PDF in subsequent panels (figures 13(b–d)) is modified by the combined effects of velocity divergence and baffle interactions. Notably, the shaping observed in figure 13(b) results from the "Neutraliser II HR" baffle, the outline in figure 13(c) is due to the "Inter-tank duct entry" baffle, and the circular outline in figure 13(d) arises from the "Duct 1 entry" baffle (see Table A.4 for baffle names and coordinates).

Figure 14 illustrates the variation in transmission efficiency with distance from the beam source, calculated using *method 0*. Step-wise reductions in efficiency are induced by baffles, resulting in a final transmission efficiency of $\eta = 93.2\%$ at the plasma cavity. The most significant degradations occur at the "Neutraliser II HR" baffle (u = 1.840m), the "Inter-tank duct entry" baffle (u = 2.799m), and the "Duct 1 entry" baffle (u = 3.851m). These results align with calculations of transmitted power efficiency in the JET beam line, as shown in figure 8 of [26]. Although [26] does not provide specific details about the beam geometry, beam divergence and baffle geometry, the reported transmission efficiency of $\eta = 88\%$ for JET, obtained using the PINI simulator code, is reassuringly close to the value computed for MAST Upgrade.

Figure 15 compares transmission efficiency at u=7m across five model variants. The dashed line represents results from $method\ 0$, considered the most accurate representation of the neutral beam system. Other calculations employ alternative sets of basis functions as prescribed in Section 5. The findings show that as the density of basis functions changes from uniform loading to edge loading ($\rho = 1.0 \rightarrow \rho = 0.5 \rightarrow \rho = 0.3 \rightarrow \rho = 0.1$), the discrepency with the $method\ 0$ result decreases. In particular the result with $\rho = 0.1$ and 5 basis functions per axis is within 0.03% of the $method\ 0$ result. Further calculations show that for these model parameters the maximum discrepency in the transmission efficiency in the range 0 < u < 10 is 0.25%. The reason that small values of ρ improve accuracy is because the generated basis functions can better account for circular baffles; in cases where the baffles are entirely

parallel to the v- or w- axes there was no observed dependence on ρ . These results show that using five basis functions per axis (totalling 25 basis functions) results in a transmission efficiency degradation of less than 0.03% at u=7m (0.25% for u < 10m), while reducing execution time by a factor of approximately 10. It is important to note that $method\ 0$ and $method\ 1$ address similar but not identical problems. While $method\ 0$ models a non-rectangular, locally varying source distribution, $method\ 1$ assumes a rectangular source with a constant (and, in this work, non-varying) fractional power density. For $method\ 1$ the transmission efficiency is affected by the dimensions of the nominal source; the results shown in Figure 15 assumed the dimensions of the rectangular beam source extended 3mm (ie one pini half-radius) beyond the outer pini beamlets.

Figure 16 presents the horizontal PDF profile, marginalized over velocity, at u=7m and v=0m. Results are shown for *method 0* and *method 1* (ρ =0.1 with five basis functions per axis). The two cases are nearly indistinguishable, indicating that the simplified model accurately represents spatial variations in the neutral beam at this location.

Figure 17 plots the marginal velocity distributions in the wu and uv planes at u=7m. Results for $method\ 0$ and $method\ 1$ (using ρ =0.5 with five basis functions per axis) are compared. The $method\ 0$ results exhibit detailed variations reflecting the spatial distribution of beamlets on the source grid. In particular, the unusual θ -dependence in the wu plane is due to fewer beamlets on the top and bottom rows of the beamlet grid (see figure 13a). In all cases the $method\ 1$ results closely replicate the trends of the $method\ 0$ results. These plots show that the effect of superposing the spatially offset Gaussian beams results in velocity distributions that are fundamentally different to the distribution of a single Gaussian beam expressed by equation 28 (c.f. figure 8).

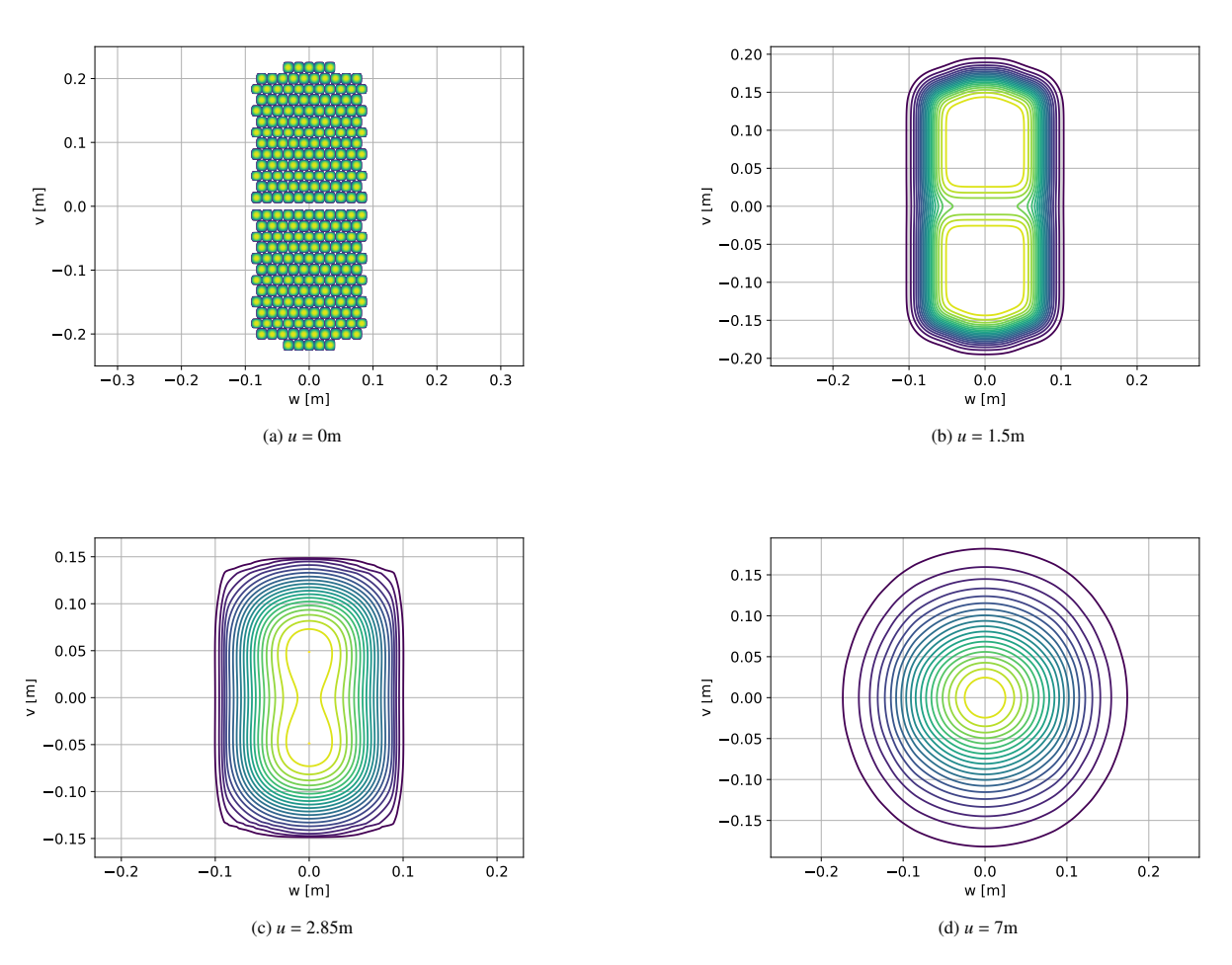


Figure 13. Variation of PDF on planes normal to the MAST Upgrade neutral beam source marginalised over velocity.

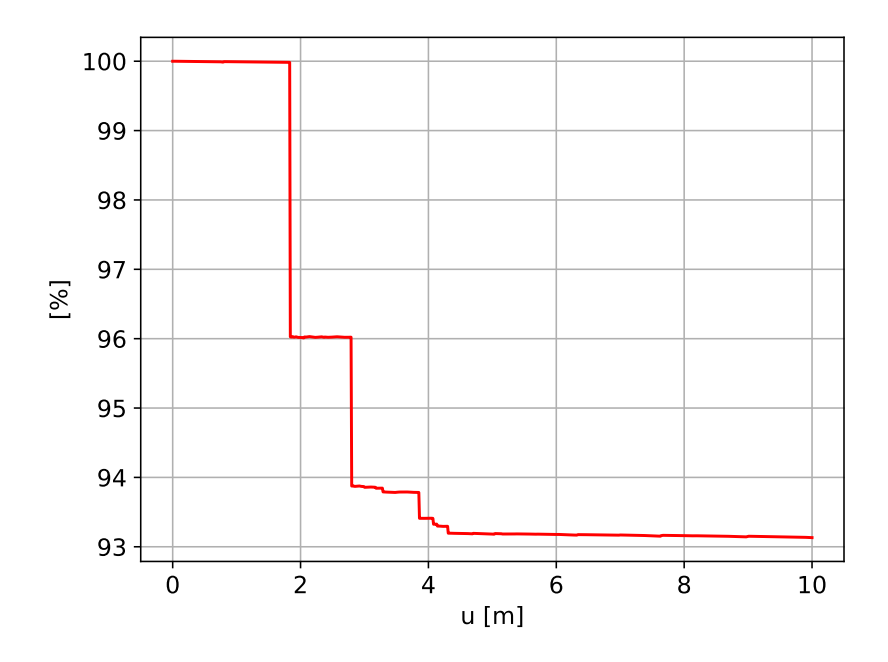


Figure 14. Variation of transmission efficiency for a MAST Upgrade neutral beam as a function of distance from the beam source.

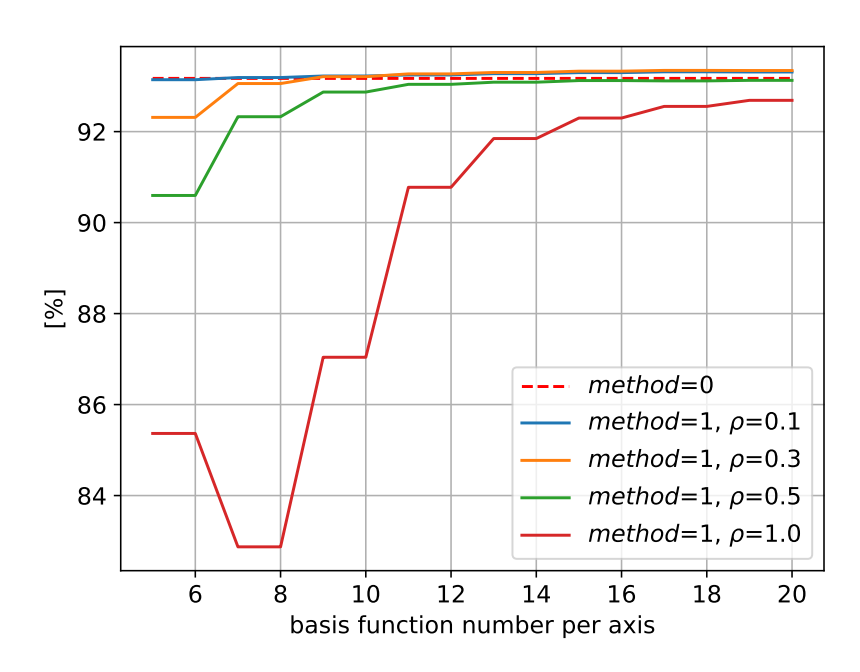


Figure 15. Comparison calculations of transmission efficiency at u=7m.

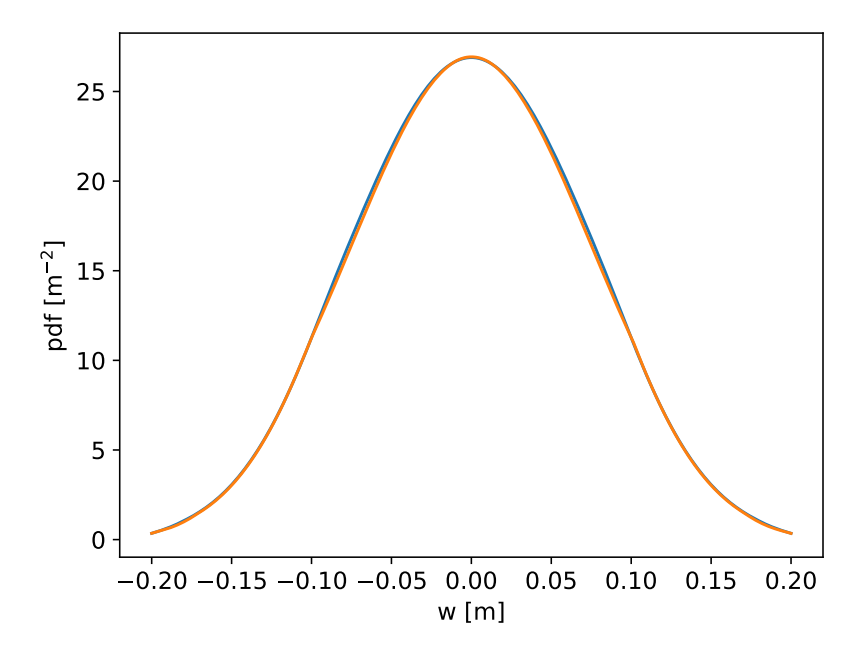


Figure 16. Horizontal profile of power density, marginalised over velocity at u=7m and v=0m.

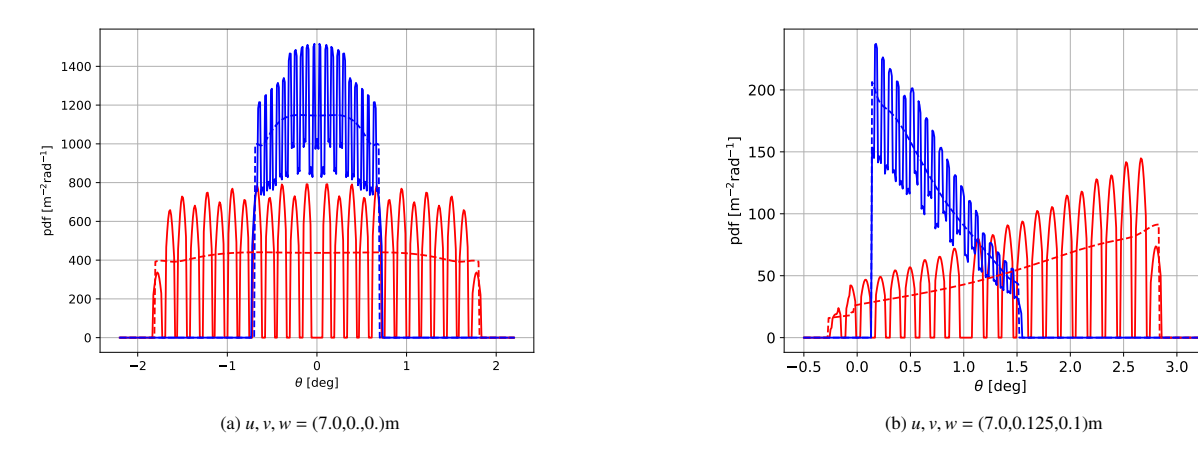


Figure 17. Marginal velocity distributions in the wu plane (blue) and in the vu plane (red). The angle θ is the anti-clockwise angle subtended by the velocity vector with the unit vector in the u-direction. Results shown are from model $method\ 0$ (solid line) and $method\ 1$ (dashed line). Refer to figure 13d to relate the velocity distributions to their spatial positions within the neutral beam.

8. Conclusions

We have developed an analytical model to describe the transport of collisionless particles in neutral beam systems, incorporating non-Gaussian source distributions using Gaussian basis functions. The model extends to two-dimensional source distributions under the assumption of separability along orthogonal axes, enabling a comprehensive analysis of beam propagation dynamics.

The model also accounts for baffle geometry, with reductions in the transmission factor due to baffle losses computed efficiently through integrals over one-dimensional marginal velocity distributions along each beam axis. The

model shows that a single beam's velocity distribution retains its Gaussian nature en route to the plasma cavity, although its divergence is modified by geometric shaping. However, superposing spatially offset Gaussian beams can produce a velocity distribution that deviates significantly from a Gaussian profile (see figure 17). The degree of deviation will depend on the spatial distribution of fractional beam power among the Gaussian components.

Our implementation of the model as a module in Minerva, interfaced with IMAS, enables the computation of two-dimensional collisionless particle distributions for any neutral beam system with an available IMAS database. Application to the MAST Upgrade neutral beam system has demonstrated the model's ability to account for detailed source distributions and to capture the evolving beam shape and velocity distribution.

A key feature of the model is its computational efficiency. By employing an analytical method to evolve the particle distribution instead of relying on Monte Carlo tracking of individual particles, the model ensures computational tractability, particularly in Bayesian analysis contexts. Using a reduced basis set to represent the source distribution maintains accuracy within 0.25% for transmission efficiency calculations, while achieving a tenfold reduction in execution time.

Future plans involve coupling the collisionless beam model with a collisional-radiative model to enhance diagnostic modelling capabilities, enabling the quantification of beam losses in the duct during its transit to the plasma cavity. Additionally, the implementation of the model within the Minerva framework, achieved during the current work, will create new opportunities to address uncertainty-related challenges in neutral beam systems within the tokamak context by utilizing the extensive Bayesian analysis tools provided by Minerva.

This integration will particularly benefit diagnostics such as Motional Stark Effect (MSE) and Charge Exchange Recombination Spectroscopy (CXRS) on MAST Upgrade. By applying Bayesian analysis, uncertainties in parameters such as beam divergence, power flux, geometry, and the neutral gas distribution in the duct can be systematically evaluated. This comprehensive approach will enhance the interpretation of diagnostic data and optimize the performance of heating systems in tokamaks reliant on neutral beams.

Acknowledgements

The Author would like to thank the useful discussions that he has had with the UKAEA neutral beam group, especially to Dave Keeling, Damian King, Ian Day, Roy McAdams and Maria Nicosia. In addition he would like to thank Sam Blackmore in the UKAEA diagnostics group, Sebastian Bannmann at IPP Greifswald and Clive Michael at the Physics and Astronomy Department, UCLA for their generous support and advice in formative discussions. Finally he would like to express sincere gratitude to Udo Hoefel and Jakob Svensson for support in the use of Minerva.

This work has been funded by the EPSRC Energy Programme [grant number EP/W006839/1]. To obtain further information on the data and models underlying this paper please contact PublicationsManager@ukaea.uk.

For the purpose of open access, the author(s) has applied a Creative Commons Attribution (CC BY) licence (where permitted by UKRI, 'Open Government Licence' or 'Creative Commons Attribution No-derivatives (CC BY-ND) licence' may be stated instead) to any Author Accepted Manuscript version arising.

Appendix A. The MAST neutral beam system

Figure A.18 shows the engineering dimensions of the The MAST neutral beam system. The values of parameters referred to in this figure are given in table A.1. Other relevant design parameters are given in table A.2. The final acceleration grid (referred to as *grid 4* in figure A.18) is shown in figure A.19. Ions emerge from 262 circular holes each with a diameter of 12mm into a neutralisation chamber. The coordinates of the sub-beamlets are provided in table A.3 and baffle coordinates in table A.4. The locations of the beam baffles are plotted in figure A.20.

References

- [1] R. Koch, Fast particle heating, Fusion Science and Technology 57 (02 2010). doi:10.13182/FST10-A9409.
- [2] E. S. Marmar, J. L. Terry, W. L. Rowan, A. J. Wootton, Diagnostic neutral beam and active spectroscopy requirements for the Alcator C-Mod tokamak, Review of Scientific Instruments 68 (1) (1997) 265–268. arXiv:https://pubs.aip.org/aip/rsi/article-pdf/68/1/265/19052982/265_1_online.pdf, doi:10.1063/1.1147821. URL https://doi.org/10.1063/1.1147821

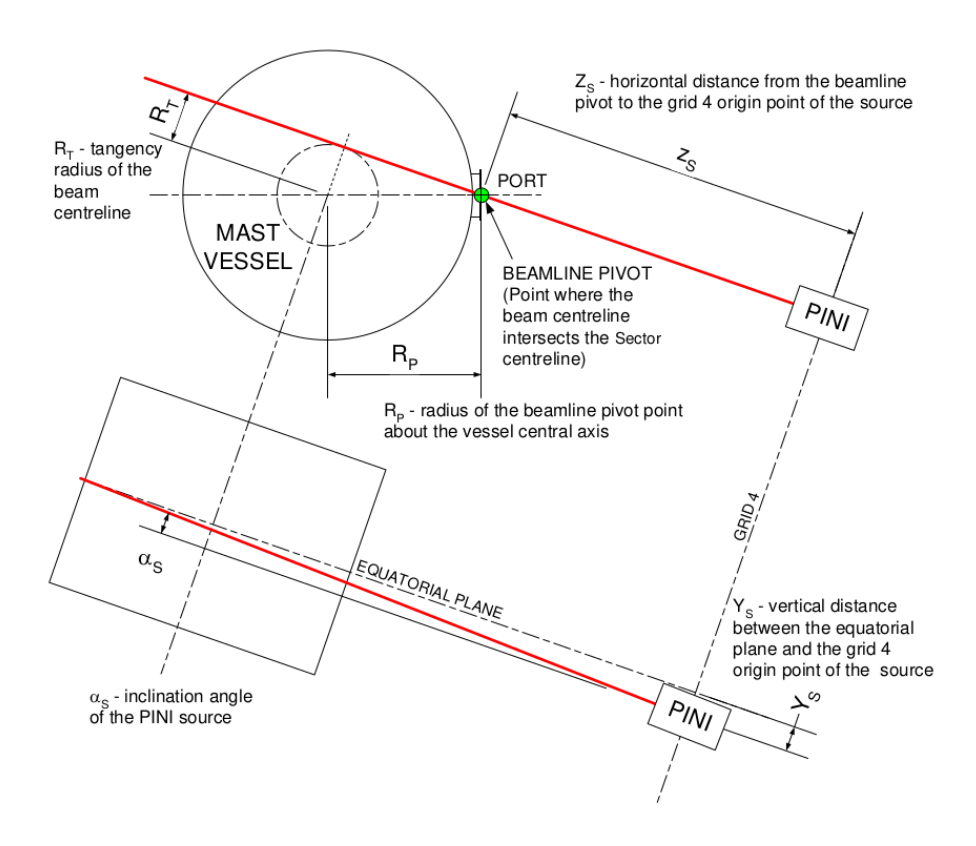


Figure A.18. "Engineering" dimensions of the MAST neutral beam system (taken from $\ [32]$).

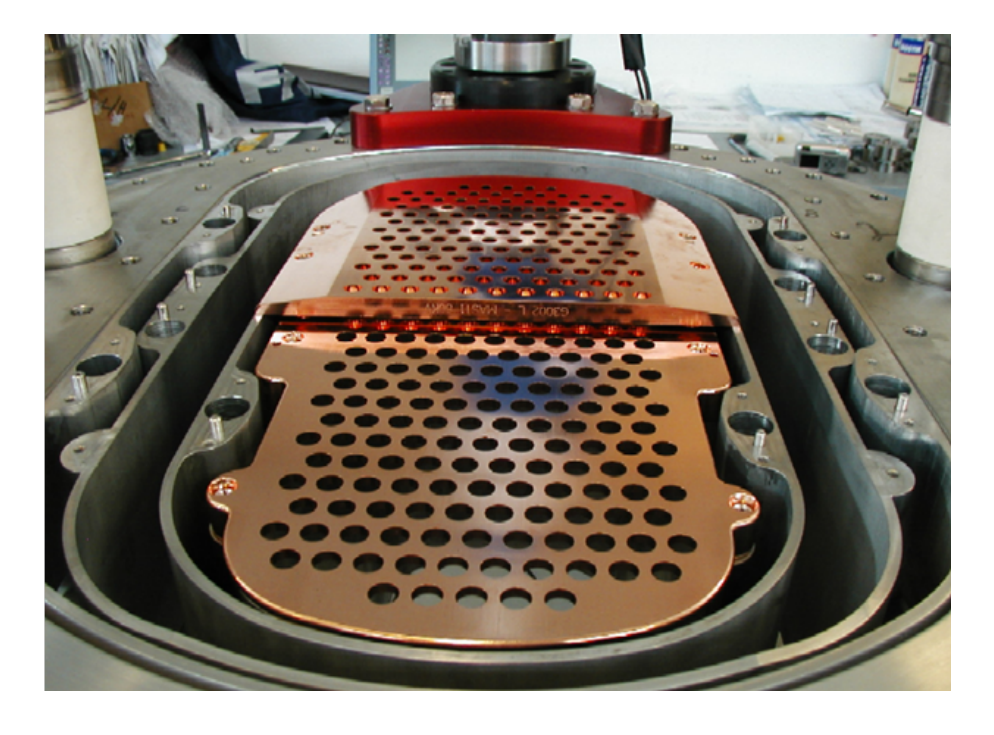


Figure A.19. "The final-stage acceleration grid (referred to as grid 4 in figure A.18). The grid consists of a lower and upper part.

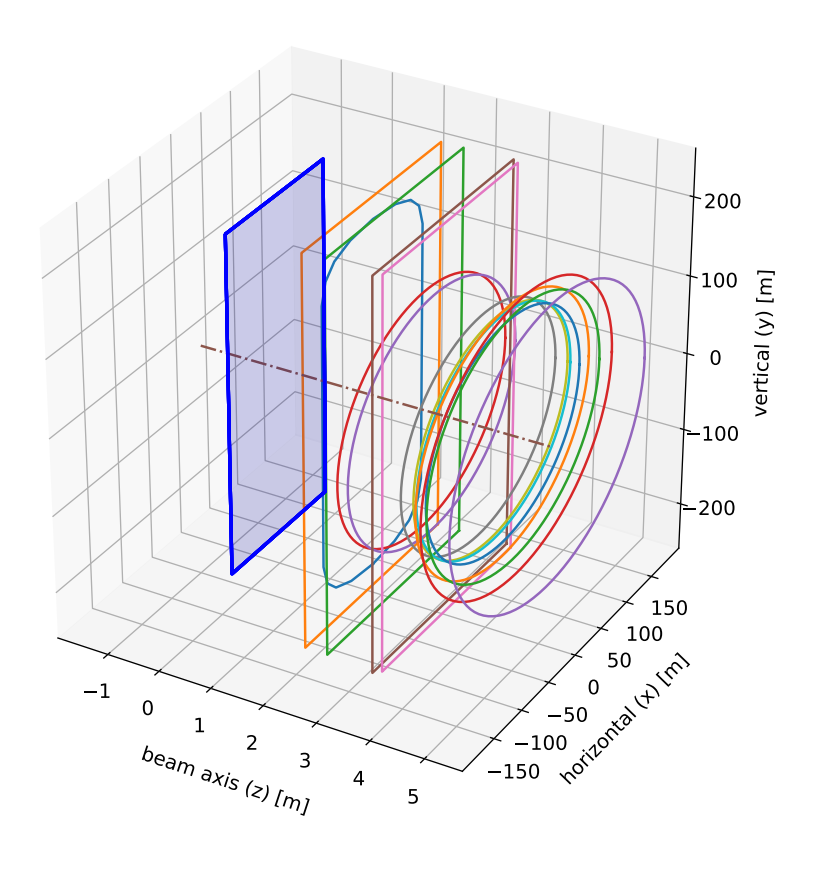


Figure A.20. Locations of the MAST Upgrade baffles. The distance from the grid at the entrance of the neutraliser (shaded blue) are shown shaded, and the beam axis is shown as a dashed brown line.

Engineering Dimension	Parameter Values / mm (unless stated)			
Engineering Dimension	sector 6	sector 8		
Beamline ID	SS	SW		
R_t Tangency radius	705.7	800		
R_p Pivot radius	2063.3	2103.5		
Z_s beamline length	5112.9	5068.3		
Y _s Vertical offset	0	650		
α_s inclination angle	0°	0°		

Table A.1. Neutral beam engineering dimensions (see figure A.18 for parameters definitions). Taken from [32].

Description	Parameter Values
Maximum beam energy	75kV
Maximum beam current	65A
Beamlet divergence angle (at maximum current and voltage)	0.6°
Grid half-height	218mm
Grid half-width	82.5mm
Horizontal focal length	14m
Vertical focal length	6m

Table A.2. Neutral beam design parameters operated with Deuterium injection. Taken from [32].

- [3] Y. Luo, W. W. Heidbrink, K. H. Burrell, E. Ruskov, W. M. Solomon, Fast-ion Dα measurements and simulations in quiet plasmas, Physics of Plasmas 14 (11) (2007) 112503. arXiv:https://pubs.aip.org/aip/pop/article-pdf/doi/10.1063/1.2794320/14048167/112503_1_online.pdf, doi:10.1063/1.2794320. URL https://doi.org/10.1063/1.2794320
- [4] G. Lister, D. Post, R. Goldston, Computer simulation of neutral beam injection into tokamaks using Monte Carlo techniques, in: Proceedings of the 3rd Symposium on Plasma Heating in Toroidal Devices, Varenna, Italy, 1976, p. 303, held in Varenna, Italy.
- [5] R. Fowler, J. Holmes, J. Rome, NFREYA -a Monte Carlo beam deposition code for non-circular tokamak plasmas, Report ORNL-TM-6845, Oak Ridge National Laboratory, TN (1979).
- [6] R. Hawryluk, An empirical approach to tokamak transport, in: B. Coppi, G. Leotta, D. Pfirsch, R. Pozzoli, E. Sindoni (Eds.), Physics of Plasmas Close to Thermonuclear Conditions, Pergamon, 1981, pp. 19-46. doi:https://doi.org/10.1016/B978-1-4832-8385-2.50009-1. URL https://www.sciencedirect.com/science/article/pii/B9781483283852500091
- [7] A. Pankin, D. McCune, R. Andre, G. Bateman, A. Kritz, The tokamak Monte Carlo fast ion module NUBEAM in the National Transport Code Collaboration library, Computer Physics Communications 159 (3) (2004) 157–184. doi:https://doi.org/10.1016/j.cpc.2003.11.002. URL https://www.sciencedirect.com/science/article/pii/S0010465504001109
- [8] M. F. M. De Bock, N. J. Conway, M. J. Walsh, P. G. Carolan, N. C. Hawkes, Ab initio modeling of the motional Stark effect on MAST), Review of Scientific Instruments 79 (10) (2008) 10F524. arXiv:https://pubs.aip.org/aip/rsi/article-pdf/doi/10.1063/1.2966459/15669786/10f524_1_online.pdf, doi:10.1063/1.2966459. URL https://doi.org/10.1063/1.2966459
- [9] O. Asunta, J. Govenius, R. Budny, M. Gorelenkova, G. Tardini, T. Kurki-Suonio, A. Salmi, S. Sipilä, Modelling neutral beams in fusion devices: Beamlet-based model for fast particle simulations, Computer Physics Communications 188 (2015) 33-46. doi:https://doi.org/10.1016/j.cpc.2014.10.024. URL https://www.sciencedirect.com/science/article/pii/S0010465514003701
- [10] B. Geiger, L. Stagner, W. Heidbrink, R. Dux, R. Fischer, Y. Fujiwara, A. Garcia, A. S. Jacobsen, A. J. van Vuuren, A. N. Karpushov, D. Liu, P. A. Schneider, I. Sfiligoi, P. Z. Poloskei, M. Weiland, Progress in modelling fast-ion d-alpha spectra and neutral particle analyzer fluxes using fidasim, Plasma Physics and Controlled Fusion 62 (10) (2020) 105008. doi:10.1088/1361-6587/aba8d7. URL https://dx.doi.org/10.1088/1361-6587/aba8d7
- [11] P. M. Stubberfield, M. L. Watkins, Multiple pencil beam, experimental Department Research Note DPA(06)87 (1987).

w	v	w	v	w w	v	w w	v	w	v	w	v
-0.0825	0.0135	-0.0825	0.1495	0.04125	0.0645	-0.066	-0.0135	-0.066	-0.1495	0.05775	-0.0645
-0.066	0.0135	-0.066	0.1495	0.05775	0.0645	-0.0495	-0.0135	-0.0495	-0.1495	0.07425	-0.0645
-0.0495	0.0135	-0.0495	0.1495	0.07425	0.0645	-0.033	-0.0135	-0.033	-0.1495	-0.07425	-0.0985
-0.033	0.0135	-0.033	0.1495	-0.07425	0.0985	-0.0165	-0.0135	-0.0165	-0.1495	-0.05775	-0.0985
-0.0165	0.0135	-0.0165	0.1495	-0.05775	0.0985	0.	-0.0135	0.	-0.1495	-0.04125	-0.0985
0.	0.0135	0.	0.1495	-0.04125	0.0985	0.0165	-0.0135	0.0165	-0.1495	-0.02475	-0.0985
0.0165	0.0135	0.0165	0.1495	-0.02475	0.0985	0.033	-0.0135	0.033	-0.1495	-0.00825	-0.0985
0.033	0.0135	0.033	0.1495	-0.00825	0.0985	0.0495	-0.0135	0.0495	-0.1495	0.00825	-0.0985
0.0495	0.0135	0.0495	0.1495	0.00825	0.0985	0.066	-0.0135	0.066	-0.1495	0.02475	-0.0985
0.066	0.0135	0.066	0.1495	0.02475	0.0985	0.0825	-0.0135	0.0825	-0.1495	0.04125	-0.0985
0.0825	0.0135	0.0825	0.1495	0.04125	0.0985	-0.0825	-0.0475	-0.0825	-0.1835	0.05775	-0.0985
-0.0825	0.0475	-0.0825	0.1835	0.05775	0.0985	-0.066	-0.0475	-0.066	-0.1835	0.07425	-0.0985
-0.066	0.0475	-0.066	0.1835	0.07425	0.0985	-0.0495	-0.0475	-0.0495	-0.1835	-0.07425	-0.1325
-0.0495	0.0475	-0.0495	0.1835	-0.07425	0.1325	-0.033	-0.0475	-0.033	-0.1835	-0.05775	-0.1325
-0.033	0.0475	-0.033	0.1835	-0.05775	0.1325	-0.0165	-0.0475	-0.0165	-0.1835	-0.04125	-0.1325
-0.0165	0.0475	-0.0165	0.1835	-0.04125	0.1325	0.	-0.0475	0.	-0.1835	-0.02475	-0.1325
0.	0.0475	0.	0.1835	-0.02475	0.1325	0.0165	-0.0475	0.0165	-0.1835	-0.00825	-0.1325
0.0165	0.0475	0.0165	0.1835	-0.00825	0.1325	0.033	-0.0475	0.033	-0.1835	0.00825	-0.1325
0.033	0.0475	0.033	0.1835	0.00825	0.1325	0.0495	-0.0475	0.0495	-0.1835	0.02475	-0.1325
0.0495	0.0475	0.0495	0.1835	0.02475	0.1325	0.066	-0.0475	0.066	-0.1835	0.04125	-0.1325
0.066	0.0475	0.066	0.1835	0.04125	0.1325	0.0825	-0.0475	0.0825	-0.1835	0.05775	-0.1325
0.0825	0.0475	0.0825	0.1835	0.05775	0.1325	-0.0825	-0.0815	-0.033	-0.2175	0.07425	-0.1325
-0.0825	0.0815	-0.033	0.2175	0.07425	0.1325	-0.066	-0.0815	-0.0165	-0.2175	-0.07425	-0.1665
-0.066	0.0815	-0.0165	0.2175	-0.07425	0.1665	-0.0495	-0.0815	0.	-0.2175	-0.05775	-0.1665
-0.0495	0.0815	0.	0.2175	-0.05775	0.1665	-0.033	-0.0815	0.0165	-0.2175	-0.04125	-0.1665
-0.033	0.0815	0.0165	0.2175	-0.04125	0.1665	-0.0165	-0.0815	0.033	-0.2175	-0.02475	-0.1665
-0.0165	0.0815	0.033	0.2175	-0.02475	0.1665	0.	-0.0815	-0.07425	-0.0305	-0.00825	-0.1665
0.	0.0815	-0.07425	0.0305	-0.00825	0.1665	0.0165	-0.0815	-0.05775	-0.0305	0.00825	-0.1665
0.0165	0.0815	-0.05775	0.0305	0.00825	0.1665	0.033	-0.0815	-0.04125	-0.0305	0.02475	-0.1665
0.033	0.0815	-0.04125	0.0305	0.02475	0.1665	0.0495	-0.0815	-0.02475	-0.0305	0.04125	-0.1665
0.0495	0.0815	-0.02475	0.0305	0.04125	0.1665	0.066	-0.0815	-0.00825	-0.0305	0.05775	-0.1665
0.066	0.0815	-0.00825	0.0305	0.05775	0.1665	0.0825	-0.0815	0.00825	-0.0305	0.07425	-0.1665
0.0825	0.0815	0.00825	0.0305	0.07425	0.1665	-0.0825	-0.1155	0.02475	-0.0305	-0.07425	-0.2005
-0.0825	0.1155	0.02475	0.0305	-0.07425	0.2005	-0.066	-0.1155	0.04125	-0.0305	-0.05775	-0.2005
-0.066	0.1155	0.04125	0.0305	-0.05775	0.2005	-0.0495	-0.1155	0.05775	-0.0305	-0.04125	-0.2005
-0.0495	0.1155	0.05775	0.0305	-0.04125	0.2005	-0.033	-0.1155	0.07425	-0.0305	-0.02475	-0.2005
-0.033	0.1155	0.07425	0.0305	-0.02475	0.2005	-0.0165	-0.1155	-0.07425	-0.0645	-0.00825	-0.2005
-0.0165	0.1155	-0.07425	0.0645	-0.00825	0.2005	0.	-0.1155	-0.05775	-0.0645	0.00825	-0.2005
0.	0.1155	-0.05775	0.0645	0.00825	0.2005	0.0165	-0.1155	-0.04125	-0.0645	0.02475	-0.2005
0.0165	0.1155	-0.04125	0.0645	0.02475	0.2005	0.033	-0.1155	-0.02475	-0.0645	0.04125	-0.2005
0.033	0.1155	-0.02475	0.0645	0.04125	0.2005	0.0495	-0.1155	-0.00825	-0.0645	0.05775	-0.2005
0.0495	0.1155	-0.00825	0.0645	0.05775	0.2005	0.066	-0.1155	0.00825	-0.0645	0.07425	-0.2005
0.066	0.1155	0.00825	0.0645	0.07425	0.2005	0.0825	-0.1155	0.02475	-0.0645		
0.0825	0.1155	0.02475	0.0645	-0.0825	-0.0135	-0.0825	-0.1495	0.04125	-0.0645		

Table A.3. Centroid locations of the 262 sub-beamlets in w,v (width and height) coordinates on the final acceleration grid. Coordinate are shown with respect to the the centre of the grid.

- [12] J. Mandrekas, Physics models and user's guide for the neutral beam module of the SUPERCODE, report GTFR-102, Georgia Institute of Technology, Atlanta (1992).
- [13] Y. Feng, B. Wolle, K. Hübner, New, simplified technique for calculating particle source rates due to neutral beam injection into tokamaks, Computer PhysicsCommunications 88 (1995) 161–172.
- [14] M. Schneider, L.-G. Eriksson, I. Jenkins, J. Artaud, V. Basiuk, F. Imbeaux, T. Oikawa, JET-EFDA contributors, ITM-TF contributors, Simulation of the neutral beam deposition within integrated tokamak modelling frameworks, Nuclear Fusion 51 (6) (2011) 063019. doi:10.1088/0029-5515/51/6/063019. URL https://dx.doi.org/10.1088/0029-5515/51/6/063019
- [15] J. Artaud, V. Basiuk, F. Imbeaux, M. Schneider, J. Garcia, G. Giruzzi, P. Huynh, T. Aniel, F. Albajar, J. Ané, A. Bécoulet, C. Bourdelle, A. Casati, L. Colas, J. Decker, R. Dumont, L. Eriksson, X. Garbet, R. Guirlet, P. Hertout, G. Hoang, W. Houlberg, G. Huysmans, E. Joffrin, S. Kim, F. Köchl, J. Lister, X. Litaudon, P. Maget, R. Masset, B. Pégourié, Y. Peysson, P. Thomas, E. Tsitrone, F. Turco, The cronos suite of codes for integrated tokamak modelling, Nuclear Fusion 50 (4) (2010) 043001. doi:10.1088/0029-5515/50/4/043001. URL https://dx.doi.org/10.1088/0029-5515/50/4/043001

Component	u	w/radius	v
	1840	0.0	-222
	1840	39.0	-218
	1840	66.0	-208
	1840	81.0	-192
	1840	87.5	-166
	1840	87.5	166
	1840	81.0	192
	1840	66.0	208
Neutraliser II HR	1840	39.0	218
	1840	0.0	222
	1840	-39.0	218
	1840	-66.0	208
	1840	-81.0	192
	1840	-87.5	166
	1840	-87.5	-166
	1840	-81.0	-192
	1840	-66.0	-208
	1840	-39.0	-218
	1840	120.0	-250
	1840	120.0	250
Magnet entry	1840	-120.0	250
	1840	-120.0	-250
	2260	120.0	-250
	2260	120.0	250
Magnet exit	2260	-120.0	250
	2260	-120.0	-250
Inter-tank duct entry	2799	150.0	_
Inter-tank duct exit	2991	150.0	_
	3171	122.0	-250
C-1	3171	122.0	250
Calorimeter element 1	3171	-125.0	250
	3171	-125.0	-250
	3289	118.0	-250
Calorimeter element 2	3289	118.0	250
Calorimeter element 2	3289	-119.0	250
	3289	-119.0	-250
Duct 1 entry	3851	140.0	_
Duct 1 exit	4080	140.0	
Duct 2 entry	4133	140.0	_
Duct 2 exit	4304	140.0	_
Duct 3 entry	4305	158.0	_
Duct 3 exit	4504	158.0	_
Duct 4 entry	4575	175.0	_
Duct 4 exit	5142	180.0	

Table A.4. Description of the fifteen baffles for each neutral beam line. The baffle outlines are given, either as a set of (w, v) coordinates or as a radius. In the case of radius the baffle outline is in a plane parallel to the source grid. The first number in each column is the distance from the source. Dimensions are given in mm.

^[16] G. Falchetto, D. Coster, R. Coelho, B. Scott, L. Figini, D. Kalupin, E. Nardon, S. Nowak, L. Alves, J. Artaud, V. Basiuk, J. P. Bizarro, C. Boulbe, A. Dinklage, D. Farina, B. Faugeras, J. Ferreira, A. Figueiredo, P. Huynh, F. Imbeaux, I. Ivanova-Stanik, T. Jonsson, H.-J. Klingshirn, C. Konz, A. Kus, N. Marushchenko, G. Pereverzev, M. Owsiak, E. Poli, Y. Peysson, R. Reimer, J. Signoret, O. Sauter, R. Stankiewicz, P. Strand, I. Voitsekhovitch, E. Westerhof, T. Zok, W. Zwingmann, ITM-TF Contributors, the ASDEX Upgrade Team, JET-EFDA Contributors, The european integrated tokamak modelling (itm) effort: achievements and first physics results, Nuclear Fusion 54 (4) (2014) 043018. doi:10.1088/0029-5515/54/4/043018.

URL https://dx.doi.org/10.1088/0029-5515/54/4/043018

^[17] M. Tournianski, Experimental investigation of ion behaviour on the START tokamak, Ph.D. thesis, The University of Essex (1999).

- [18] S. Bannmann, O. Ford, U. Hoefel, P. Poloskei, A. Pavone, S. Kwak, J. Svensson, S. Lazerson, P. McNeely, N. Rust, D. Hartmann, E. Pasch, G. Fuchert, R. Wolf, the the W7-X-Team, Fast forward modeling of neutral beam injection and halo formation including full balmer-α emission prediction at w7-x, Journal of Instrumentation 18 (10) (2023) P10029. doi:10.1088/1748-0221/18/10/P10029. URL https://dx.doi.org/10.1088/1748-0221/18/10/P10029
- [19] S. Bannmann, O. Ford, U. Hoefel, P. Z. Poloskei, A. Pavone, S. Kwak, J. Svensson, S. Lazerson, P. McNeely, N. Rust, D. Hartmann, E. Pasch, G. Fuchert, A. Langenberg, N. Pablant, K. J. Brunner, R. C. Wolf, the W7-X Team, Bayesian inference of electron density and ion temperature profiles from neutral beam and halo balmer-α emission at wendelstein 7-x, Plasma Physics and Controlled Fusion 66 (6) (2024) 065001. doi:10.1088/1361-6587/ad3c1d. URL https://dx.doi.org/10.1088/1361-6587/ad3c1d
- [20] D. A. Homfray, D. Ciric, V. Dunkley, R. King, D. Payne, M. R. Simmonds, B. Stevens, P. Stevenson, C. Tame, S. E. V. Warder, A. M. Whitehead, D. Young, Overview of MAST neutral beam system performance, in: 2009 23rd IEEE/NPSS Symposium on Fusion Engineering, 2009, pp. 1–4. doi:10.1109/FUSION.2009.5226423.
- [21] A. Holmes, R. McAdams, Space charge compensation of positive ion beams used in magnetic fusion applications, Nuclear Fusion 62 (6) (2022) 066017. doi:10.1088/1741-4326/ac544c. URL https://dx.doi.org/10.1088/1741-4326/ac544c
- [22] P. Veltri, E. Sartori, P. Agostinetti, D. Aprile, M. Brombin, G. Chitarin, N. Fonnesu, K. Ikeda, M. Kisaki, H. Nakano, A. Pimazzoni, K. Tsumori, G. Serianni, Ion beam transport: modelling and experimental measurements on a large negative ion source in view of the ITER heating neutral beam, Nuclear Fusion 57 (1) (2016) 016025. doi:10.1088/0029-5515/57/1/016025. URL https://dx.doi.org/10.1088/0029-5515/57/1/016025
- [23] E. Surrey, C. Challis, D. Ciric, S. Cox, B. Crowley, I. Jenkins, T. Jones, D. Keeling, Measurement of the depletion of neutraliser target due to gas heating in the JET neutral beam injection system, Fusion Engineering and Design 73 (2) (2005) 141–153. doi:https://doi.org/10.1016/j.fusengdes.2005.06.348.
 URL https://www.sciencedirect.com/science/article/pii/S0920379605003832
- [24] D. B. King, C. D. Challis, E. G. Delabie, D. Keeling, G. F. Matthews, A. Shepherd, S. Silburn, JET contributors, Neutral beam injection on JET: Effect on neutron discrepancy and energy balance, in: 45th EPS Conference on Plasma Physics, Vol. 352, Prague, 2018, paper number: P4 1067
- [25] D. King, R. Sharma, C. Challis, A. Bleasdale, E. Delabie, D. Douai, D. Keeling, E. Lerche, M. Lennholm, J. Mailloux, G. Matthews, M. Nicassio, Ž. Štancar, T. Wilson, JET Contributors, Tritium neutral beam injection on JET: calibration and plasma measurements of stored energy, Nuclear Fusion 63 (11) (2023) 112005. doi:10.1088/1741-4326/acee97.
 URL https://dx.doi.org/10.1088/1741-4326/acee97
- [26] D. Ciric, J. Milnes, E. Surrey, Influence of accelerator grid misalignment on multi-aperture particle beam properties, in: Proceedings of the 19th IEEE/IPSS Symposium on Fusion Engineering. 19th SOFE (Cat. No.02CH37231), 2002, pp. 56–59. doi:10.1109/FUSION.2002.1027641.
- [27] D. Ciric, H. D. Falter, D. J. Godden, Space and time resolved doppler spectroscopy of neutral beams, in: B. Beaumont, P. Libeyre, B. de Gentile, G. Tonon (Eds.), Proceedings of the 20th Symposium on Fusion Technology (SOFT 1998), Association Euratom-CEA Cadarache, Saint-Paul-Lez-Durance, France, 1999, pp. 469–472, published in Fusion Technology 1998.
 URL https://scipub.euro-fusion.org/wp-content/uploads/2014/11/JETC98040.pdf
- [28] D. Godden, Plasma non-uniformity in the JET neutral beam injection source measurement, simulations and development of an improved source, Ph.D. thesis, Dublin City University (2000).
 URL https://doras.dcu.ie/18755/1/Daniel_J_Godden.pdf
- [29] D. J. Godden, D. Ciric, H. D. Falter, Modelling ion source uniformity, in: Proceedings of the 21st Symposium on Fusion Technology (SOFT), Madrid, Spain, 2000.
- [30] D. J. Godden, D. Ciric, H. D. Falter, Modelling ion source uniformity, https://scipub.euro-fusion.org/wp-content/uploads/ 2014/11/EFDC00111.pdf, downloadable report corresponding to the presentation at the 21st Symposium on Fusion Technology (Madrid, Spain, 2000). Accessed: 2025-01-20 (2000).
- [31] G. Duesing, H. Altmann, H. Falter, A. Goede, R. Haange, R. S. Hemsworth, P. Kupschus, D. Stork, E. Thompson, Neutral beam injection system, Fusion Technology 11 (1) (1987) 163–202. arXiv:https://doi.org/10.13182/FST87-A25004, doi:10.13182/FST87-A25004. URL https://doi.org/10.13182/FST87-A25004
- [32] T. Barrett, Neutral beam physics and beamline position parameters, Design Process CD/MU/00038, UK Atomic Energy Authority, updated: 19th July 2012 (July 2012).
- [33] J. Svensson, A. Werner, Large scale bayesian data analysis for nuclear fusion experiments, in: 2007 IEEE International Symposium on Intelligent Signal Processing, 2007, pp. 1–6. doi:10.1109/WISP.2007.4447579.
- [34] S. D. Pinches, J.-F. Artaud, F. J. Casson, Progress in the ITER integrated modelling programme and the ITER scenario database, in: Proceedings of the 27th IAEA Fusion Energy Conference (FEC 2018), International Atomic Energy Agency (IAEA), IAEA-CN-258, Ahmedabad, India, 2018, p. 504.
- [35] ITER organisation, Contains publicly accessible ITER repositories on github, https://github.com/iterorganization, accessed: 2025-01-20 (2025).
- [36] T. R. Barrett, C. Jones, P. Blatchford, B. Smith, R. McAdams, N. Woods, Engineering design of the double neutral beam injection system for MAST Upgrade, Fusion Engineering and Design 86 (6) (2011) 789-792, proceedings of the 26th Symposium of Fusion Technology (SOFT-26). doi:https://doi.org/10.1016/j.fusengdes.2011.01.020.
 URL https://www.sciencedirect.com/science/article/pii/S0920379611000329